Article

Metabolic Modeling Elucidates Phenformin and Atpenin A5 as Broad-Spectrum Antiviral Drugs

Alina Renz[1,#], Mirjam Hohner[2,#], Maximilian Breitenbach[2], Jonathan Josephs-Spaulding[3,§], Johanna Dürrwald[2], Lena Best[3], Raphaël Jami[2], Georgios Marinos[3], Filipe Cabreiro[4] Andreas Dräger[1,5,6,7,$,*], Michael Schindler[2,$,*]and Christoph Kaleta[3,$,*]

1. Computational Systems Biology of Infections and Antimicrobial-Resistant Pathogens, Institute for Bioinformatics and Medical Informatics (IBMI), Eberhard Karl University of Tübingen, 72076 Tübingen, Germany
2. Institute for Medical Virology and Epidemiology of Viral Diseases, University Hospital Tübingen, 72076 Tübingen, Germany
3. Research Group Medical Systems Biology, Institute of Experimental Medicine,Christian-Albrechts-University Kiel & University Hospital Schleswig Holstein, 24105 Kiel, Germany
4. Cologne Excellence Cluster for Cellular Stress Responses in Aging-Associated Diseases (CECAD), University of Cologne, 50931 Cologne, Germany
5. Department of Computer Science, Eberhard Karl University of Tübingen, 72076 Tübingen, Germany
6. German Center for Infection Research (DZIF), partner site Tübingen, Germany
7. Cluster of Excellence 'Controlling Microbes to Fight Infections,' Eberhard Karl University of Tübingen, 72076 Tübingen, Germany

# These authors contributed equally
$ These authors contributed equally
§ Present address: The Novo Nordisk Foundation Center for Biosustainability, Technical University of Denmark, 2800 Kgs. Lyngby, Denmark
* Correspondence: c.kaleta@iem.uni-kiel.de, michael.schindler@med.uni-tuebingen.de, andreas.draeger@uni-tuebingen.de

Abstract: The SARS-CoV-2 pandemic has reemphasized the urgent need to develop broad-spectrum antiviral therapies. We developed a computational pipeline that uses scRNA-Seq data to reconstruct the metabolic state of cells and tissues during viral infection. Using this pipeline, we investigated the cellular capacity to produce SARS-CoV-2 virions in various tissues and disease conditions. Subsequently, we expanded our analysis to influenza A and dengue virus and identified several metabolic targets and their inhibitors for broad-spectrum antiviral treatment. Phenformin, an inhibitor of NADH:ubiquinone oxidoreductase, suppressed SARS-CoV-2 and dengue virus replication. Using Atpenin A5 to block the succinate dehydrogenase inhibited SARS-CoV-2, dengue virus, influenza A virus and respiratory syncytial virus with superior therapeutic indices. Thus, our work establishes host metabolism as druggable for broad antiviral therapy. Moreover, our pipeline, the identified targets, and inhibitors are invaluable tools for pandemic preparedness.

Keywords: Drug discovery; Systems biology; SARS-CoV-2; Dengue; Influenza A; RSV; cell viability analysis; antivirals

Introduction

In December 2019, the outbreak of a novel coronavirus (CoV) from a seafood market in Wuhan, China, became public. This novel virus was alarmingly similar to the Severe Acute Respiratory Syndrome virus (SARS-CoV), responsible for a global outbreak in 2002 and 2003 [1]. In 2012, another coronavirus spread in the Middle East, causing the Middle East Respiratory Syndrome (MERS), leading to 2,458 reported cases and a high mortality rate of 35% [2]. History shows that pandemics repeatedly plagued humankind. In the last 100 years alone, there have been four major influenza pandemics and multiple epidemics, including the Spanish flu in 1918 with an estimated 17 to 50 million deaths worldwide [3] as well as the Asian and Hong Kong flu in 1957/58 and 1968/69 with one to four million deaths worldwide [4]. Pandemics are not only virus-driven: One of the most extensive pandemics was the Black Death from 1331 to 1353, caused by the bacterium *Yersinia pestis* and is estimated to have killed approximately half of Europe's population [5].

Thus, pandemics and epidemics are recurrent, and more are likely to follow in the future, in particular due to human impact on the global environment in the context of climate change [6]. Moreover, the COVID-19 pandemic illustrates their substantial impact on long-term socioeconomic well-being due to the widespread and long-lasting consequences of efforts of pathogen containment [7] and the occurrence of post-acute sequelae such as long COVID [8]. Therefore, the rapid development of effective treatment strategies and vaccines is vital to mitigate those consequences. However, despite the unprecedented acceleration in the development of treatment and vaccination approaches against SARS-CoV-2, it still took approximately ten months before vaccine approval to treat SARS-CoV-2 and another 6-8 months before production and distribution pipelines became functional for a widespread roll-out. Thus, treatment approaches which contain viral replication of not only single but a broad array of viruses as first-line therapeutic approaches for novel emergent pathogens are a highly sought-after goal in preparation for future pandemics [9]. Nowadays, efforts to provide such broadly acting antivirals are summarized under the term pandemic preparedness.

In this work, we developed a computational pipeline to integrate a generic metabolic model of a virally infected cell with transcriptomic data to predict metabolic pathways relevant for viral replication (Fig. 1A). Using SARS-CoV-2 as our primary study case, we used a variety of single-cell sequencing data sets to investigate differences in the cellular capacity to produce SARS-CoV-2 virions across tissues and disease stages. We found considerable differences in viral replication capacity across tissues and that infection with SARS-CoV-2 has profound effects on viral replication capacity in uninfected cells. Subsequently, we expanded our scope to two additional human pathogenic viruses to identify metabolic reactions that could serve as druggable targets for broad-spectrum antiviral compounds while not impeding cellular viability. We identified several such targets in central metabolism and compounds known to inhibit them. Through testing those compounds in cellular infection assays, we demonstrate their capability to inhibit viral replication without severe adverse effects on cell survival. These results demonstrate our pipeline's feasibility for identifying broad-spectrum antiviral compounds in preparation for future emergent pathogens.

Results

Modeling of SARS-CoV-2 infected cells reveals tissue-specific differences in viral replication capacity

In an initial step, we globally assessed cellular viral replication capacity across cell types that express the SARS-CoV-2 entry receptors *ACE2* and *TMPRSS2* (referred to as SARS-CoV-2 permissive cell types). To this end, we reconstructed context-specific models based on the human metabolic network Recon 2.2 [10] extended by a SARS-CoV-2-specific viral replication reaction [11] (see Methods). We used *StanDep* pre-processed scRNA-seq data for all cell types in the Tabula Muris Senis data set [12] as input for the fastcore algorithm [13] (see Methods) to build the context-specific models. We used this mouse data set as the basis for an unbiased comparison of viral replication capacities across cell types while avoiding potential bias inherent in human data from post mortem tissues [14,15]. Subsequently, we predicted viral replication capacity for each cell using flux balance analysis [11] (see Methods).

Among SARS-CoV-2 permissive cell types, we observed a broad range of viral replication capacities (Fig. 1B). The highest viral replication capacities were observed for the intestine and cells of the oral cavity, which is in line with observations of viral replication in those tissues [16–18]. Since the mouse data did not include the small intestine, which is the primary site of viral replication in the gastrointestinal tract [19], we additionally used scRNA-seq data from humans covering the gastrointestinal tract [20]. Here, we found the highest viral replication capacities in transit-amplifying (TA) cells across all tissues and enterocytes of the ileum (Fig. 1C). In the respiratory tract, we observed the highest viral replication capacity in alveolar type II pneumocytes, even though it was relatively small compared with other cell types (Fig. 1B). We confirmed similar viral replication capacities in the upper respiratory tract of humans, including ciliated cells, which are considered the primary targets of SARS-CoV-2 infection [21,22] (Fig. 1D). Notable further examples of SARS-CoV-2 permissive cell types with high viral replication rates are cells of the skin and brain pericytes. These observations are in agreement with observations of skin lesions in approximately 60% of COVID-19 patients [23] and brain pericytes representing a potential entry portal for brain infection [24], as well as the high frequency of neurological symptoms in COVID-19 patients [25].

SARS-CoV-2 infection induces a pro-viral state in non-infected bystander cells.

Next, we investigated how active SARS-CoV-2 infection impacted predicted viral replication capacity based on scRNA-Seq data from COVID-19 patients [26]. In contrast to the upper respiratory tract of uninfected individuals, viral replication capacity in this compartment was strongly increased (Fig. 2A). During infection, both ciliated and secretory cells showed a mean increase in the predicted viral replication rate by a factor of 2 and 3, respectively. Both cell types are the primary site of cellular infection in the upper respiratory tract [21,22]. Also FOXN4 cells, which were only detected in infected individuals[26], showed a similar high viral replication capacity. Of note, these changes were not attributable to active viral replication, since most cells in the dataset were negative for SARS-CoV-2 RNA. This indicates that viral infection of a particular cell has pleiotropic effects on non-infected bystander cells, making them much more permissive to viral infection. Investigating changes in cellular metabolic activity in these cells, we found strong induction of a large number of metabolic pathways in non-infected cells of COVID-19 patients, which was even more pronounced in patients with severe disease (Fig. 2B). Thus, 55 of the 57 analyzed metabolic pathways were significantly different between infected individuals and healthy controls and 39 metabolic pathways were significantly different between patients with moderate and severe disease.

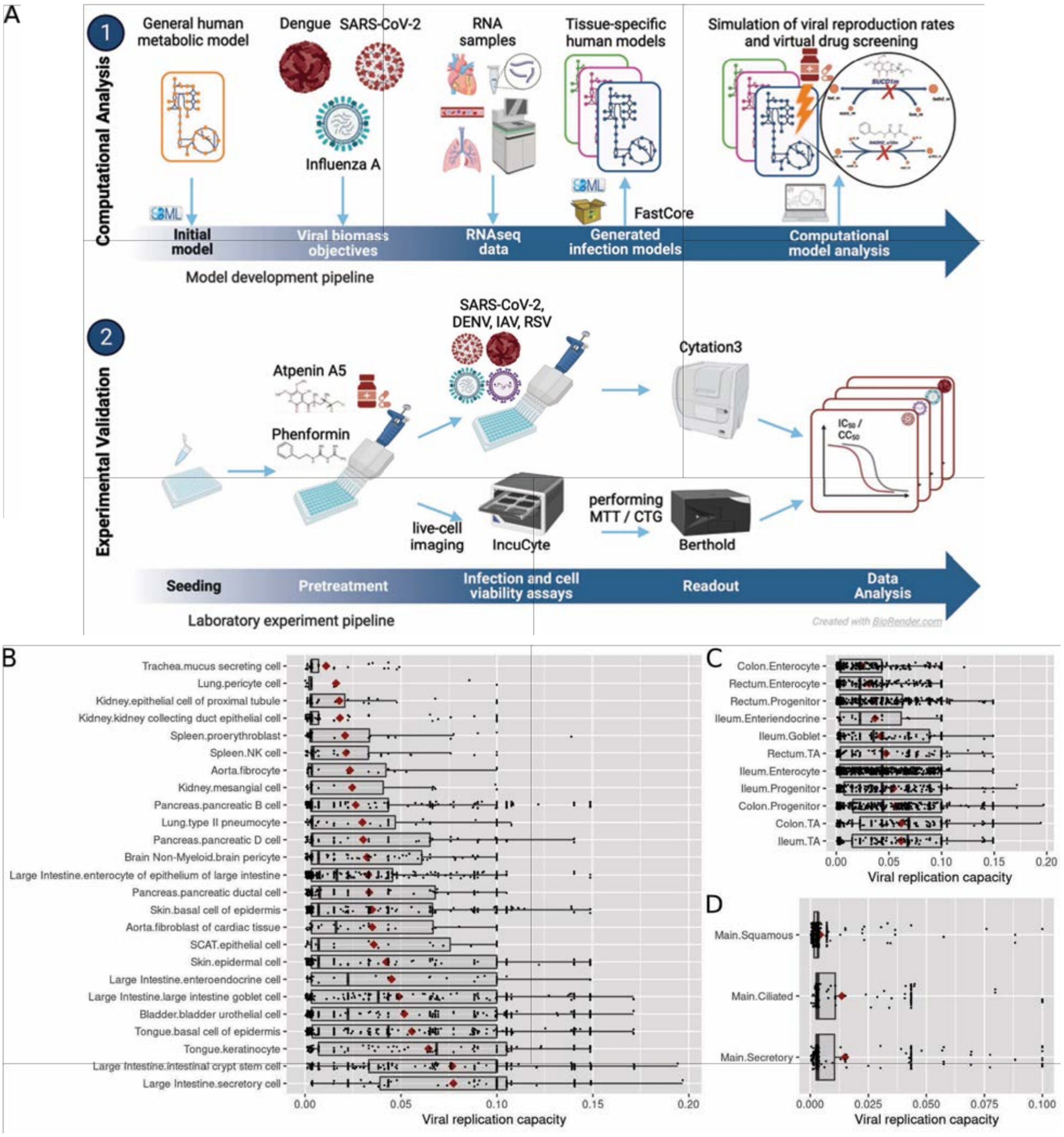

Figure 1 | Workflow and viral replication capacity of SARS-CoV-2 across cell types. **A** Model reconstruction approach and experimental validation. **B** Viral replication capacity in mice across SARS-CoV-2 permissive cell types. Diamonds indicate the means of the distribution. Tissues of origin precede cell types separated by a dot. **C** Viral replication capacity in SARS-CoV-2 permissive cell types of the human intestine. **D** Viral replication capacity in SARS-CoV-2 permissive cell types of the human lung.

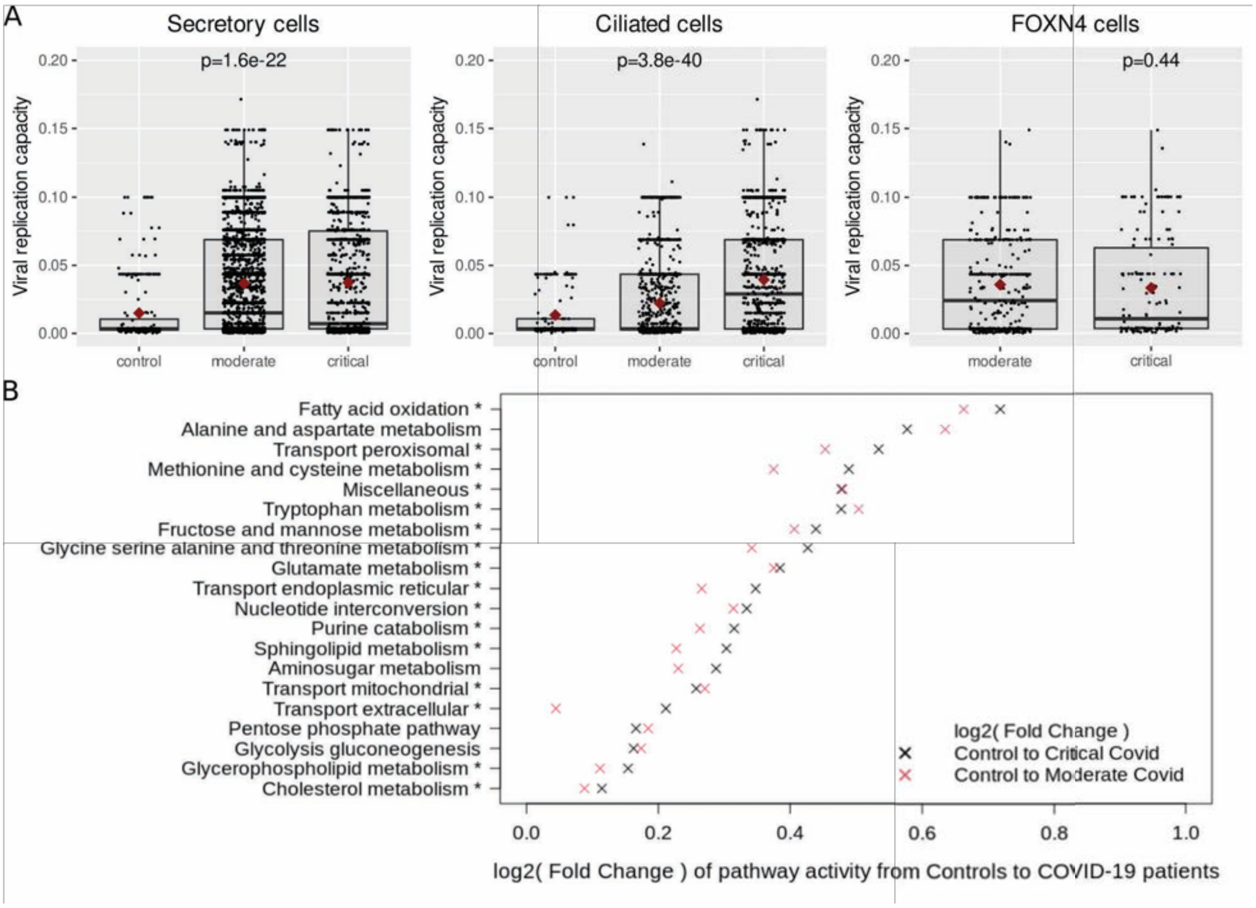

Figure 2 I Impact of disease state on predicted viral replication capacity of SARS-CoV-2 during infection. **A** Differences in viral replication capacity according to disease severity in SARS-CoV-2 permissive cell types of the lung. Please note that FOXN4-positive cells were only detected in infected individuals. **B** Cellular metabolism is strongly induced in the respiratory tract of COVID-19 patients. Metabolic models built from throat swab and lung lavage scRNA-Seq data from SARS-CoV-2 infected individuals were analyzed. Only cells where no viral RNA was detected were considered (="uninfected cells"). Pathways with significantly different activity between moderate to severe COVID-19 patients are marked with an asterisk. The 20 pathways with the most pronounced effects are shown. For the full list of pathways see Supplementary Table S1.

Enzymes essential for viral replication are enriched among the interactome of several classes of human-pathogenic viruses.

In the next step, we used our metabolic models to identify potential metabolic targets to inhibit viral replication. Besides SARS-CoV-2, we included influenza A and dengue as two prototypic RNA viruses with high human-pathogenic potential in our analysis to identify potential broad-spectrum antiviral targets. For the identification of druggable targets, we considered three classes of enzymes: "tier-1 targets", "tier-2 targets", and "other enzymes." Tier-1 targets correspond to enzymes whose knockout impedes viral replication while having only a minimal impact on the simulated cellular viability. In contrast, the knockout of tier-2 targets inhibits viral replication and impacts normal cellular metabolism. While it is in principle not advisable to impede normal cellular metabolism, anti-viral treatments are typically expected to be provided only in the short term during the acute phase of infection. Hence, tier-2 targets follow a similar strategy like chemotherapeutics which often impair normal cellular metabolic activity. Finally, enzymes not belonging to either group are categorized as "other enzymes." We separated enzymes into these three classes for each dataset and virus using flux balance analysis (see Methods). We hypothesized that the proteome of the viruses should preferentially interact with enzymes relevant for its replication without harming cellular viability and hence, be considered as tier-1 targets. In line with this assumption, for all three viruses, we observed a highly significant enrichment of known interaction partners of the viral proteome among tier-1 targets compared to tier-2 targets and all other enzymes (Fig. 3).

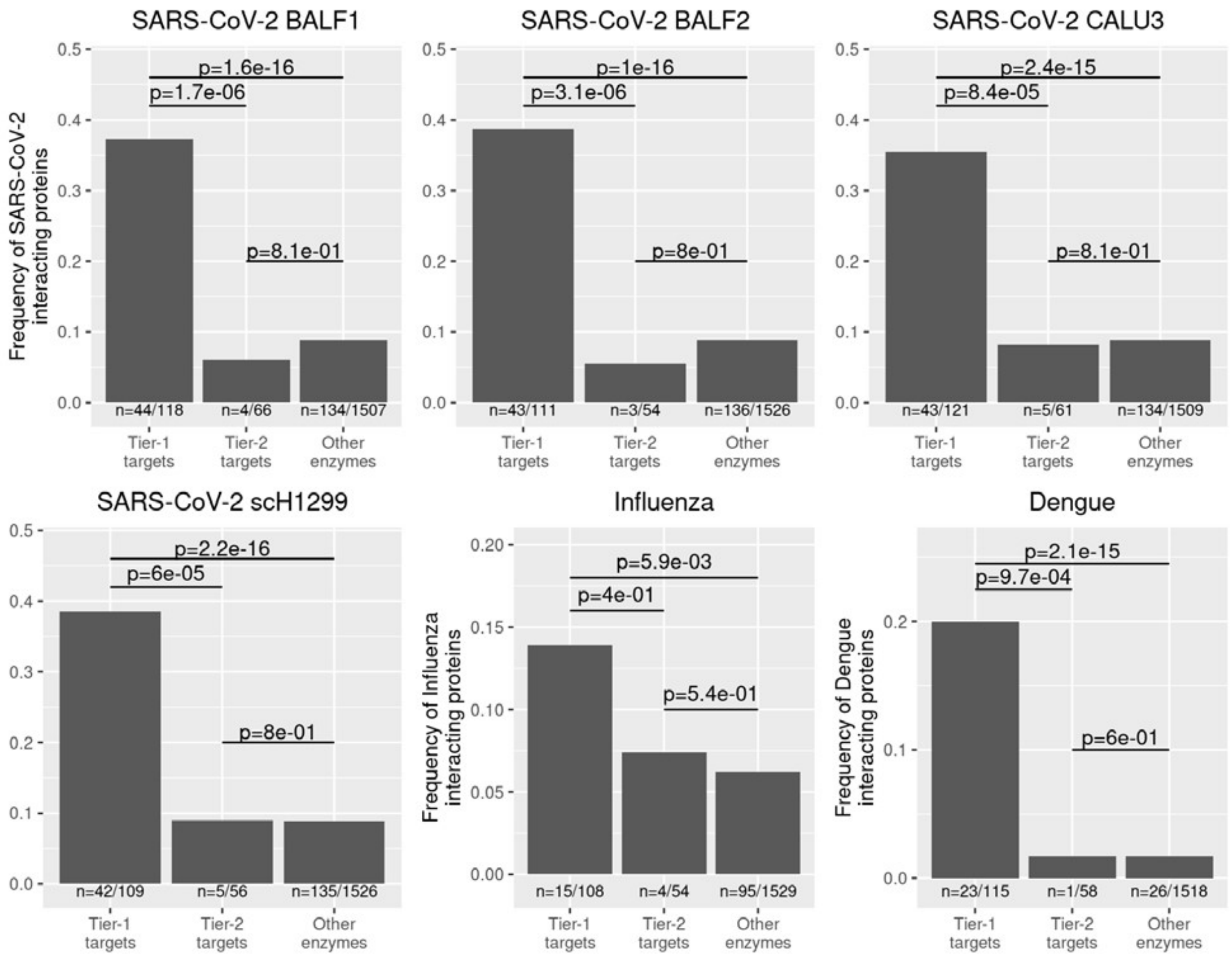

SARS-CoV-2 BALF1

SARS-CoV-2 BALF2

SARS-CoV-2 CALU3

SARS-CoV-2 scH1299

Influenza

Dengue

Figure 3 | Enrichment of viral interaction partners among enzymes relevant for viral replication in SARS-CoV-2, dengue virus, and influenza A virus. For each dataset, the fraction of genes that are experimentally-determined interaction partners of the viral proteomes among tier-1 targets and tier-2 targets occurring in at least 5% of all cells of a dataset that had tier-1 targets was determined. *P*-values were corrected for multiple testing using false discovery rate control. The number of interacting proteins relative to the number of all proteins in each category is shown below each bar. For the host-virus-interaction data set as well as the list of tier-1 and tier-2 targets for each data set see Supplementary Tables S2 and S3. ScRNA-Seq datasets: SARS-CoV-2, BALF1 [27]; SARS-CoV-2, BALF2 [26]; SARS-CoV-2, CALU-3 cell culture [28]; SARS-CoV-2, scH1299 cell culture [28]; influenza H1N1 [29], Human airway epithelia (MucilAirTM) [30]; dengue, PBMC, [31]. Protein-protein-interaction datasets: SARS-CoV-2 [32]; dengue virus [33]; influenza A virus [34].

Identification of drug targets for broad-spectrum antiviral therapy

Following our identification of tier-1 targets that inhibit the individual viruses, we sought to identify potential broad-spectrum antiviral targets. To this end, we collected all predicted tier-1 targets across all cells from the individual datasets (Supplementary Table S3) and identified 254 enzymes that occurred as a tier-1 target across all datasets. Using the BioGRID database[35] as reference, we find that interactions of 158 of these targets with human pathogenic viruses have been reported before, which represents a highly significant enrichment among reported interactions between enzymes and viruses (Fisher's exact test p-value=9.1×10^{-12}, odds ratio 1.9-3.4) and supports their central role in viral replication across diverse viruses. To further subselect our targets, we required that each target had a confirmed interaction with at least two of the three considered viruses. Thus, we obtained a list of 39 potential targets belonging to 22 proteins/protein complexes (Supplementary Table S4). Among those 39 targets, 26 interacted with further viruses than the three considered in our analysis (Supplementary Table S4).

Among those 21 protein complexes, we selected four which encompass 11 of the 39 enzyme targets for further experimental validation based upon additional criteria such as evidence from CRISPR-Cas screens, relevance in other viral diseases, and the availability of inhibitors. These four protein complexes are the NADH:ubiquinone oxidoreductase complex (complex I of the respiratory chain), the succinate dehydrogenase complex (complex II of the respiratory chain), CDP-diacylglycerol-inositol 3-phosphatidyltransferase and solute carrier family 16 member 1.

Eight targets correspond to various subunits of NADH:ubiquinone oxidoreductase across which protein-protein interactions with all three viruses have been observed (Supplementary Material S4). Moreover, interactions of NADH:ubiquinone oxidoreductase subunits with respiratory syncytial virus (RSV) [36], human immunodeficiency virus 1 (HIV-1) [37], human gammaherpesvirus 8 (HHV-8) [38], human papillomavirus (HPV) serotype 18 [39], hepatitis C virus (HCV) [40] and Nipah virus [41] have been reported. An approved drug to inhibit NADH:ubiquinone oxidoreductase is the biguanide metformin [42], the first-line treatment in type II diabetes mellitus [42]. Intriguingly, previous observational studies have shown reduced mortality of type II diabetic patients taking metformin during COVID-19 [43]. The aim to improve the effect of metformin led to the development of phenformin [44] which shows an improved cellular uptake compared to metformin [45] and was used in the downstream experiments. The solute carrier family 16 member 1 gene (SLC16A1), a monocarboxylic acid-transporter, interacts with SARS-CoV-2 and influenza A virus proteins. It was additionally identified as an interaction partner of HCV [46] and demonstrated to be a relevant host factor for SARS-CoV-2 infections in two CRISPR-Cas knockout screens [47,48]. SR13800 was identified as a potential inhibitor of SLC16A1 [49,50]. The succinate-ubiquinone oxidoreductase subunit A (SDHA) is part of complex II of the respiratory chain and catalyzes the reaction of succinate to fumarate in the tricarboxylic acid cycle. Besides its interaction with SARS-CoV-2 [32,47], SDHA also interacts with the Epstein-Barr virus (EBV) [39], the influenza A virus [51], HCV [52], and HHV-8 [38]. Atpenin A5 is a known SDHB inhibitor [53] and was previously assessed for its therapeutic effect on cardiac injury in isolated perfused rat hearts [54]. The CDP-diacylglycerol-inositol 3-phosphatidyltransferase (CDIPT), is involved in the biosynthesis of phosphatidylinositol. It interacts with the SARS-CoV-2 and influenza A proteome and is reported in three CRISPR-Cas studies as a relevant host factor during SARS-CoV-2 infection [47,48,55].

CDIPT also interacts with proteins of numerous HPV serotypes [39,56], EBV [39] and HIV-1[57]. Scyllo-inositol is listed as an inhibitor of CDIPT [58] and was proposed as a potential drug to prevent Alzheimer's disease [59].

doi:10.20944/preprints202210.0223.v1

Experimental validation of broad-spectrum antivirals in viral infection assays

The antiviral activity of the identified compounds phenformin, atpenin A5, SR13800, and scyllo-inositol was first tested in the lung cell line Calu-3 and the colon cell line CaCo-2 infected with SARS-CoV-2 (Fig. 4). The infection rate was measured by virus-encoded reporter gene expression (mNeonGreen) 48 hours after infection. The cell viability was assessed by Hoechst staining of the nucleus (see methods) and hence assessment of total cell numbers after 72 hours of treatment. Phenformin and atpenin A5 inhibited SARS-CoV-2 infection of Calu-3 cells at different doses and also partly of Caco-2 cells, whereas SR13800 showed toxicity at higher concentrations and scyllo-inositol did not show any activity (Fig. 4A and representative primary images in Fig. 4B).

Phenformin and atpenin A5 showed antiviral activity against mNeonGreen expressing SARS-CoV-2, which is based on an early Wuhan isolate (Fig. 4). Since both compounds were identified by us *in silico* as potential broadly acting antivirals, we assessed their IC_{50} in inhibiting SARS-CoV-2 including a recent Omicron variant, dengue virus (DENV), the respiratory syncytial virus (RSV) and influenza A virus (IAV) (Fig. 5A) and the CC_{50} based on total cell numbers (Fig. 5B). Phenformin had an IC_{50} of 1.46 μM and atpenin A5 an IC_{50} of 0.45 μM against the original Wuhan strain in Calu-3 cells without cellular toxicity and both compounds were similarly active against the Omicron variant. This observation indicates that it is active against all currently circulating variants of concerns. It was previously reported that type II diabetic patients taking metformin, similar to phenformin, showed a reduced risk of severe COVID-19 compared to non-users [43]. We therefore also included metformin in our SARS-CoV-2 infection experiments revealing that it inhibited infection only at very high concentrations at an IC_{50} of 459 μM in Calu-3 cells, again without showing any cytotoxicity (Fig. 5 and Supp. Fig. 1).

Phenformin had an IC_{50} of 17.15 μM against DENV in Huh7.5 hepatoma cell lines, while atpenin A5 inhibited DENV infection at an IC_{50} of 0.36 μM (Fig. 5A and Supp. Fig. 1). Of note, atpenin A5 also inhibited RSV and IAV infection of the lung cell line A549 at IC_{50}s of 0.14 μM (IAV) and 0.12 μM (RSV), respectively (Fig. 5A and Supp. Fig. 1). Phenformin was inactive against RSV and IAV at the concentrations tested. Of note, we did not measure severe cytotoxicity of any of the compounds in the three cell lines tested (Fig. 5B).

doi:10.20944/preprints202210.0223.v1

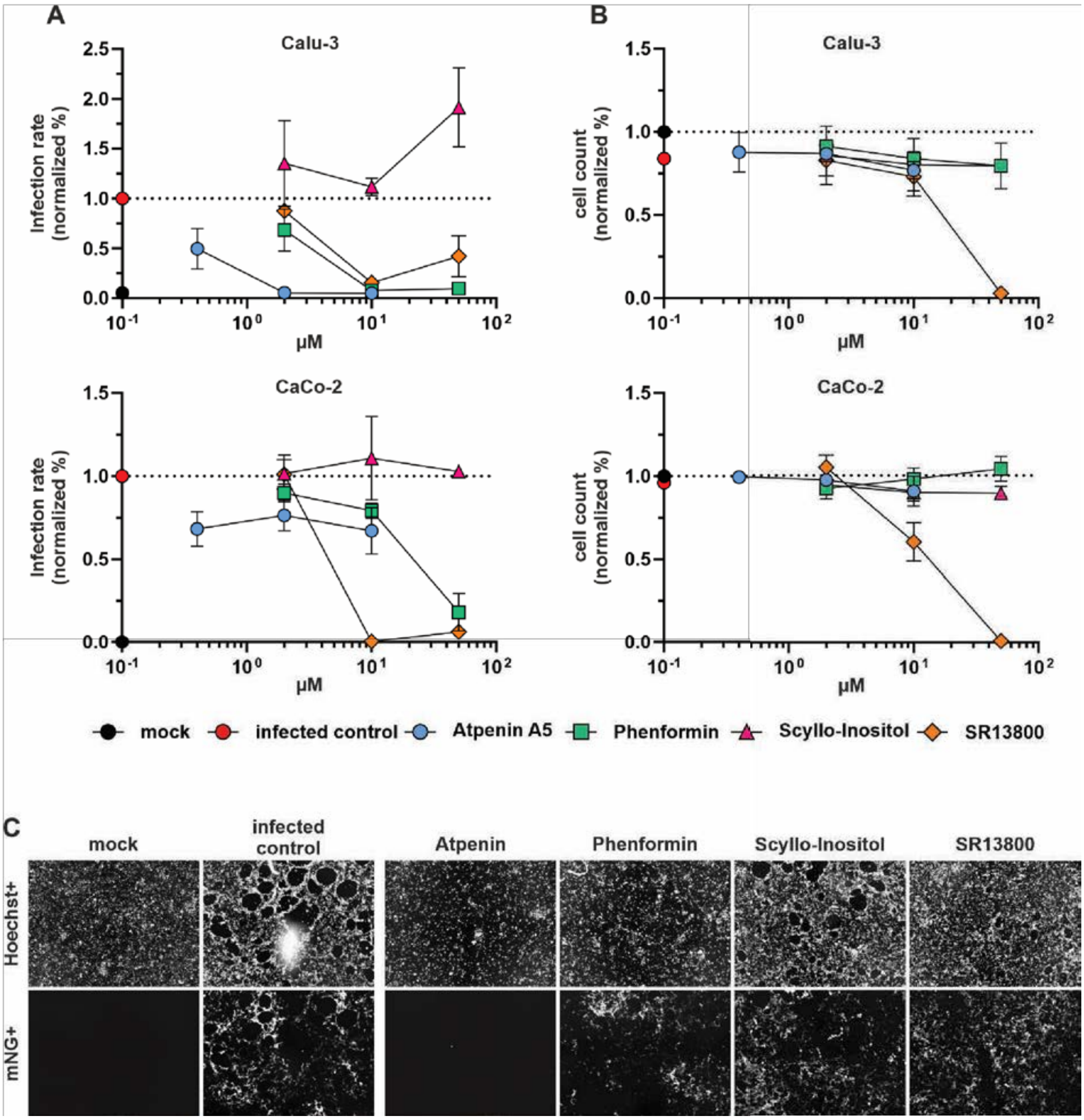

Figure 4 | Atpenin A5 and phenformin show antiviral activity against SARS-CoV-2. Calu-3 and CaCo-2 cells were pre-treated for 24 hours with atpenin A5, phenformin, scyllo-inositol and SR13800 in indicated concentrations and infected with icSARS-CoV-2-mNG. 48 hours post infection, cells were fixed, stained with Hoechst and measured with a Cytation3 multiplate imager. **A** Infection rate (mNG+/Hoechst+ cells) normalized to untreated infected cells. **B** Cell count (Hoechst+ cells) normalized to mock. n=3. Data represent means ± S.E.M. **C** Representative fluorescence microscopy images were taken at 4-fold magnification to detect cell nuclei count (Hoechst+), and infected cells count (mNeonGreen+).

doi:10.20944/preprints202210.0223.v1

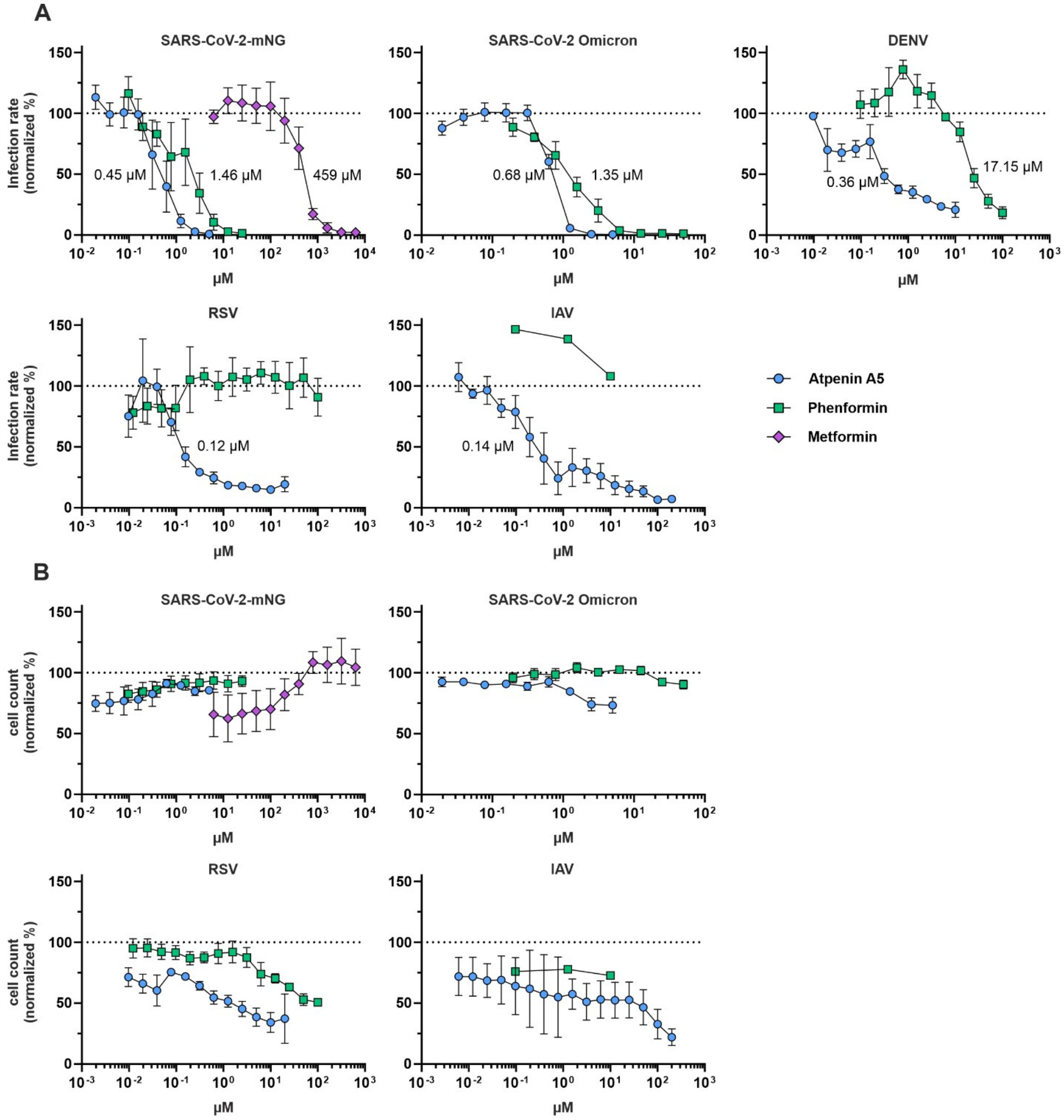

Figure 5 | IC$_{50}$ determination against different RNA viruses in various cell lines of atpenin A5 and phenformin. Atpenin A5 and phenformin were tested for antiviral activity against two different SARS-CoV-2 strains, icSARS-CoV-2-mNG and the variant of concern Omicron, a respiratory syncytial reporter virus (RSV) and an influenza A reporter virus (IAV) expressing GFP as well as an luciferase expressing dengue reporter virus. Cells were pre-treated with the compounds for 24 hours, respectively for 1 hour (DENV). 48 hours post infection cells were fixed, stained with Hoechst and measured with Cytation3 multiplate reader. DENV infected cells were lysed for measuring luciferase activity. **A** Graphs show infection rate normalized to untreated infected cells. µM values in the graphs refer to the specific IC_{50} values. **B** Cell count (Hoechst+ cells) normalized to mock. n=3; n=2 (IAV, atpenin A5); n=1 (IAV, phenformin). Data represent means ± S.E.M.

Detailed analysis of atpenin A5 and phenformin cytotoxicity and inhibition of metabolic activity in various cell lines.

As predicted from our modeling as tier 1 targets, atpenin A5 at 20 µM and phenformin at 100 µM do not show toxicity in end point measurements based on total cell counting when Calu-3, CaCo-2, A549 and Huh7.5 cells were exposed to the compounds for 72 hours (Fig. 4 and Fig. 5). However, since cell counting is only a rough proxy to assess cytotoxicity and a higher dose escalation is necessary for CC_{50} counting, we further included careful determination of growth kinetics by live cell imaging, measurement of mitochondrial metabolic activity by MTT assay as well as cellular ATP levels by CellTiter-Glo (CTG, see material and methods section for details). The data is summarized in Fig. 6. Careful titration of atpenin A5 indicated CC_{50} values based on growth curve assessment in Calu-3 cells > 160 µM, 65 µM in Huh7.5 and 40.3 µM in A549 cells (Fig. 6A). In comparison, phenformin showed much less impairment of cell growth with a CC_{50} of 1500 µM in Calu-3 and 1115 µM in Huh7.5 cells (Fig. 6B). As expected, since MTT and CTG assays measure cellular metabolism, the CC_{50} values of both compounds were somehow lower in the various cell types as compared to growth curve assessment and can be interpreted as a surrogate for the compounds on-target activity (Fig. 6C). CC_{50} values measured for atpenin A5 based on MTT and CTG closely mimic the IC_{50}, with 3.6 µM (MTT) and 1.0 µM (CTG), respectively. Apparently, the other cell types, i.e. Huh7.5 and A549 seem to have more active metabolic pathways showing only modest impairment in MTT and CTG in the presence of atpenin A5. Similarly, phenformin showed a lower on-target activity in both assays as compared to atpenin A5 (Fig. 6C), which might also be reflected by its higher IC_{50} values.

Finally, the careful determination of the IC_{50} (Fig. 5) and CC_{50} (Fig. 6) allowed us to calculate the therapeutic indices (TI) of atpenin A5 and phenformin against different viruses in the various cell lines (Table 1). From this, we conclude that atpenin A5 is a potent antiviral that inhibits SARS-CoV-2, DENV, IAV and RSV with TIs throughout > 100 when considering growth kinetics as the most relevant assay to determine impairment of cellular viability. Phenformin potently inhibited SARS-CoV-2 and DENV while it was not active against IAV and RSV. Altogether, this data shows that phenformin and atpenin A5 are antivirals active against several non-related viruses and support the suitability of our pipeline to identify broad-spectrum antiviral drugs and targets.

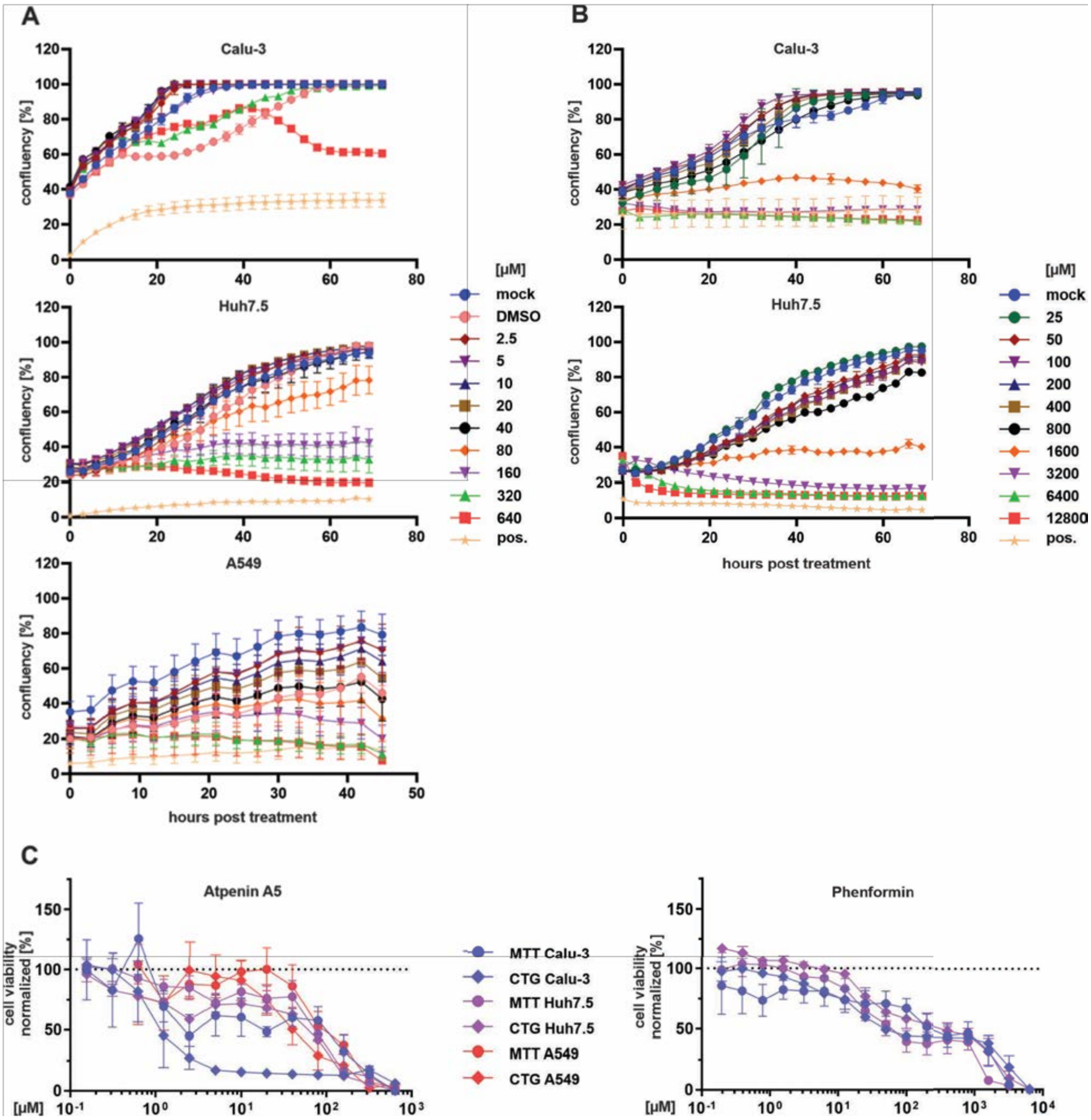

Figure 6 | Effects of atpenin A5 and phenformin on the growth and viability of various cell lines. Calu-3, Huh7.5 and A549 cells were treated with the indicated concentrations of **A** atpenin A5 and **B** phenformin for 48 hours (A549) or 72 hours (Calu-3, Huh7.5). DMSO (1.3 %) is a solvent control. The positive control is 50 % DMSO to inhibit cell growth. Plates were imaged in the IncuCyte® at 37 °C, 5 % CO_2, every 3 to 4 hours to assess cell confluency. For analysis IncuCyte® S3 Software was used. Number of replicates: Calu-3, n=1; Huh7.5, n=2 / 3; A549, n=5. Data represent means ± interplate S.E.M. **C** Cellular metabolic activity was measured using CellTiter-Glo® or MTT assay as described in the material and methods section. Graphs show normalized MTT signal to non-treated cells or normalized luminescence signal to non-treated cells. n=3; Data represent means ± S.E.M.

Atpenin A5	**IC_{50}**	**CC_{50}**	**therapeutic index: CC_{50}/IC_{50}**
ic-SARS-CoV-2-mNG (in Calu-3 cells)	0.45 μM	MTT: 3.6 μM CTG: 1.0 μM IncuCyte: > 160 μM	MTT: 8 CTG: 2.2 IncuCyte: > 355
SARS-CoV-2 omicron (in Calu-3 cells)	0.68 μM	MTT: 3.6 μM CTG: 1.0 μM IncuCyte: > 160 μM	MTT: 5.3 CTG: 1.5 IncuCyte: > 235
Dengue Virus (in Huh7.5 cells)	0.36 μM	MTT: 83.3 μM CTG: 85.4 μM IncuCyte: 65 μM	MTT: 231.4 CTG: 258.8 IncuCyte: 180.6
Influenza A Virus (in A549 cells)	*0.14 μM (n=2)*	MTT: 114.7 μM CTG: 49.5 μM Incucyte: 40.3 μM	*MTT: 819.3* *CTG: 353.6* *Incucyte: 287.9*
RSV (in A549 cells)	0.12 μM	MTT: 114.7 μM CTG: 49.5 μM IncuCyte: 40.3 μM	MTT: 955.8 CTG: 412.5 Incucyte: 335.8
Phenformin	**IC_{50}**	**CC_{50}**	**therapeutic index: CC_{50}/IC_{50}**
ic-SARS-CoV-2-mNG (in Calu-3 cells)	1.46 μM	MTT: 456 μM CTG: 26.3 μM IncuCyte: 1500 μM	MTT: 312.3 CTG: 18.0 IncuCyte: 1027.4
SARS-CoV-2 omicron (in Calu-3 cells)	1.35 μM	MTT: 456 μM CTG: 26.3 μM IncuCyte: 1500 μM	MTT: 337.8 CTG: 19.5 IncuCyte: 1111.1
Dengue Virus (in Huh7.5 cells)	17.15 μM	MTT: 64.2 μM CTG: 80.2 μM IncuCyte: 1115 μM	MTT: 3.7 CTG: 4.7 IncuCyte: 65.0
Influenza A Virus (in A549 cells)	*not active*		
RSV (in A459 cells)	*not active*		

Table 1 I Therapeutic indices of atpenin A5 and phenformin against various pandemic RNA viruses in different cell lines.

Discussion

In this work, we have used constraint-based metabolic modeling in combination with single-cell sequencing data to investigate the metabolic state of virally infected cells and identify potential targets for broad-spectrum antiviral treatment. Based on our modeling approach, we found considerable differences in the predicted cellular capacity to produce virions, with the highest predicted replication rates observed in the colon and parts of the oral cavity. In contrast, cells of the upper respiratory tract seemed to sustain SARS-CoV-2 replication to a relatively low extent. Accordingly, a high frequency of patients that shed their virus via feces has been observed, even long after clearance of the virus in the respiratory tract [60]. Interestingly, intestinal tissue shows minor pathology during active viral infection [61]. Despite this high capacity for viral replication *in silico* and *in vivo*, the fecal-oral route is a relatively uncommon transmission mode for SARSCoV-2, likely due to the rapid inactivation of virions by luminal fluids [19]. While cells of the upper respiratory tract show a relatively low baseline of metabolic SARS-CoV-2 replication capacity in the healthy state, this capacity is considerably increased upon infection. Thus, SARS-CoV-2 seems to prime neighboring non-infected cells for viral replication along with pronounced induction of many metabolic pathways, which we previously have also reported for several types of immune cells in COVID-19 patients [62]. It remains to be investigated whether this pleiotropic activation of metabolic pathways is a general feature across a larger number of viruses. Some of these effects might be mediated by virus-induced cellular senescence, which entails a senescence-associated secretory phenotype that induces a pro-inflammatory microenvironment upon SARS-CoV-2 infection [63]. However, it remains unclear to which extent these pleiotropic effects of viral infection are mediated via direct effects (aberrant signaling by infected cells) or indirectly via interaction of SARS-CoV-2 with the local immune system.

We further exploited our reconstructed metabolic models to identify potential targets for antiviral therapy. In order to identify druggable targets with broad antiviral activity, we expanded our analysis to two additional viruses with pandemic potential, dengue virus (DENV) a member of the Flaviviridae and the fastest growing insect-borne disease as we all as influenza A virus (IAV), belonging to the Paramyxoviridae. We categorized antiviral targets into tier-1 and tier-2 targets, depending on whether their knockout would impede viral replication but not impact normal metabolism and viability (tier-1 targets) or prevent viral replication with an impairment of cell survival (tier-2 targets). We found that the identified tier-1 targets were highly enriched among experimentally confirmed interaction partners of all three viruses. Of note, this enrichment was much more pronounced for tier-1 targets than for tier-2 targets, indicating that all three viruses dysregulate and hijack cellular proteins essential for viral replication but dispensable for cell survival. This could reflect optimal virus-host adaptation in order to maximize the production of viral progeny without killing the host cell.

Following the identification of tier-1 targets across all datasets, we identified 254 potential enzyme targets of which 158 have already been reported in association with viral proteins, which represents a highly significant enrichment. Further subsetting those targets to those which have a reported association with at least two of the three considered viruses, we identified 39 proteins forming parts of 22 protein complexes that could serve as druggable targets for broad-spectrum viral inhibition. Among those targets, we observed many proteins in the respiratory chain, notably complex I, complex II, and ATP synthase (23 out of 39 proteins). This result is in line with the critical role of the respiratory chain in viral infection, providing substrates for viral replication and acting as signaling hubs for the immune response [64]. Among those candidates, we selected four enzyme complexes comprising eleven of the identified targets for further experimental validation. Using inhibitors of those enzymes, we could confirm that targeting the NADH:ubiquinone oxidoreductase complex by phenformin and the succinate dehydrogenase by atpenin A5, blocked viral replication in cell culture experiments with minimal cellular toxicity. Remarkably, while phenformin inhibited the replication of DENV and SARS-CoV-2, atpenin A5 showed excellent antiviral activity against DENV, SARS-Cov-2, RSV and IAV. All four viruses belong to completely distinct viral taxons, thereby strongly supporting the suitability for broad-spectrum antiviral therapy. Importantly, our target prediction approach did not incorporate data from RSV infected cells, thus further supporting the notion that the predicted targets also work beyond the three viruses that were initially included in our analysis.

Phenformin was well tolerated up to high concentrations, which agrees with its previous use as an antidiabetic drug before it was withdrawn from the market in the 1970s due to deadly cases of lactic acidosis compared to the alternative antidiabetic metformin. The frequency of lactic acidosis was 40 to 64 per 100,000 patients per year and probably related to renal insufficiency similar to metformin therapy [65]. Hence, provided that treatment in the context of acute viral infections is short-termed and fundamentally different as the long-term treatment in diabetes, phenformin could represent a viable treatment option, also when monitoring the renal status of patients. Furthermore, reported plasma levels of phenformin after 50-100 mg of phenformin uptake in patients are ~1.7 µM [66], which is in the range of the IC_{50} measured against SARS-CoV-2 and levels in plasma and liver of intra-portal infused rats was ~110 µM in liver and ~40 µM in plasma [67]**.** Atpenin A5 is up to now an experimental compound, which was not tested *in vivo*, possibly due to its expectable multiple adverse effects in various organs. Atpenin A5 is known as potent complex II inhibitor [68], thus affecting the redox-chain at the mitochondrial membrane and overall energy metabolism, two features that are also reflected by our MTT and CTG assays (Fig. 6 and Table 1). Nevertheless, complex II inhibition is also discussed as a druggable metabolic pathway for various cancer types [69]. Novel atpenin A5 derived leads were developed with a much higher on target specificity [70]. These recent developments in combination with our observation that complex II inhibition via the succinate dehydrogenase is a druggable and highly potent target for broad-spectrum antiviral inhibition, raises the possibility for rapid establishment of novel broadly acting antiviral drugs.

While we have identified and validated several targets for broad-spectrum antiviral therapies, this validation has been restricted to cell culture systems. It remains to be seen whether those compounds are also viable antiviral compounds *in vivo*. Moreover, we have only explored a subset of our predicted targets, and other targets from this list might provide an even higher potency for inhibiting viral replication in a broad set of viruses. Importantly, this study provides substantial proof that targeting metabolism is a valid strategy in the context of antiviral therapies [71]. This approach has considerable advantages over classical antivirals that target virally encoded enzymes, so called directly acting antivirals, since metabolism-based targets exert a very low variability and are predictably essential for viral replication, resulting in a very high resistance barrier. In this context, our pipeline for the identification of antiviral targets integrating knowledge on cellular metabolism and data from virally infected cells as well as the inhibitors that we have identified could represent an essential tool for rapidly identifying antiviral targets. Thus, this pipeline could be an invaluable resource for pandemic preparedness against future emergent pathogens.

Methods

Computational analysis

Single-cell sequencing datasets

Table 2 summarizes the single-cell sequencing datasets that were used.

Table 2 | Single-cell sequencing datasets.

Dataset	**Reference**	**Accession Number**	**Celltype annotation source**
BALF1	[27]	GSE145926	Annotation via CHETAH version 1.8.0 with single cell lung atlas (GSE136831,[72])
BALF2	[26]	EGAS00001004481	Original authors (https://doi.org/10.6084/m9.figshare.12436517)
CALU-3	[28]	GSE148729	Single cell experiment
scH1299	[28]	GSE148729	Single cell experiment
Tabula Muris	[12]	https://tabula-muris.ds.czbiohub.org/	Original authors
Intestine	[20]	GSE125970	Original authors
Influenza H1N1	[29]	GSE191176	Manual annotation following methods of original publication
Dengue	[31]	GSE116672	Annotation via CHETAH version 1.8.0

			with PBMC single cell reference [62]

Viral replication models based on Recon 2.2

The viral biomass objective function (VBOF) for SARS-CoV-2 was taken from Renz et al. [11]. The VBOF for dengue was taken from Aller et al. [73]. No VBOF for influenza A H1N1 was available and, thus, needed to be constructed. The nucleotide and protein sequences with the RefSeq number GCF_001343785.1 were downloaded from NCBI's Reference Sequence database [74]. The genome copy number was assumed to be 1. Influenza A H1N1 has four structural proteins: hemagglutinin (HA), neuraminidase (NA), matrix protein 1 (M1), and matrix protein 2 (M2). The nonstructural proteins include the polymerases PB1, PB2, and PA, the nucleocapsid protein (NP), the nonstructural protein 1 (NS1), the nuclear export protein (NEP), and the PA-X protein (PAX). The detailed list of copy numbers for the structural and nonstructural proteins is given in Supplementary Table S6. The stoichiometric coefficients for the nucleotides, amino acids, and energy requirements were calculated based on the copy numbers and according to the steps suggested by Aller et al. [73]. These coefficients are provided in Supplementary Table S7. The genome-scale metabolic model of humans, Recon 2.2 [10], was expanded with the viral replication reaction for each of the three viruses. The model was conditioned with a medium corresponding to concentration of metabolites present in human blood (Supplementary Table S8)[62]. Subsequently, we used fastcore's fastcc algorithm and the simulated blood serum diet to generate consistent models for each virus. These models are available from the Biomodels database (see data availability).

Cell identity annotation

Cell type annotation was not available for all datasets analyzed in this study. For deposited data with missing metadata on cell identity, we performed cell type annotation *de novo* (see Supplementary Figure S2). For the datasets BALF1 and dengue, we employed the R-package CHETAH (version 1.8.0)[75]. CHETAH makes use of a reference single-cell RNA dataset which is used to build a classification tree via hierarchical clustering. Input cells are placed and identified as reference cell types or intermediate types in the classification tree.

The **BALF1 dataset** was annotated using a single cell lung atlas of idiopathic pulmonary fibrosis, chronic obstructive pulmonary disease, and healthy smoker and non-smoker's lung cells ([72], GSE136831). Only cells annotated as epithelial in the original work were considered. The **dengue dataset** was annotated using an in-house available PBMC single cell dataset [62]. References were prepared according to the CHETAH R-package manual. Briefly, annotation references were created from single-cell expression datasets with known cell type identifications. Single cells of only healthy donors were kept in the reference. Rare cell types with less than 15 cells representing that cell type were dropped from the reference. In the interest of computing times, the remaining cell types were downsampled to a maximum of 300 cells, picked at random. The remaining single cells were normalized sample-wise to an equal sequencing depth of one million, and +1 was added to each gene's count to allow for $\log_2$ transformation. For an improved classification, ribosomal and housekeeping genes were dropped (Supplementary Table S9). After creating Seurat objects and performing quality control as described in "scRNA core reaction pre-processing," cell type annotation was done on the Seurat objects. For this, the classification function CHETAHclassifier was run with the query dataset and the matching reference. The quality of the automated classification was visually controlled with dimension reduction plots.

The **influenza H1N1 dataset** was manually annotated since CHETAH provided unsatisfactory results. We followed the steps outlined in the accompanying publication's methods [29].

scRNA core reaction pre-processing

Prior to the reconstruction of single-cell metabolic models, gene expression scRNA datasets (Methods: scRNA Datasets) were accessed from NCBI's Gene Expression Omnibus (GEO)[76] for pre-processing with Seurat [77] and StanDep [78]. Seurat objects of the respective scRNA datasets were created and cells removed if data was of insufficient quality (number of detected genes > 200 and < 6,000; mitochondrial RNA with mapped reads < 10). For datasets with missing cell type information, cell identity annotation was applied to the filtered Seurat objects (see "Cell identity annotation"). Gene level counts were translated into transcripts per million (TPM) values through normalization according to human ENSEMBL gene lengths. ENSEMBL[79] gene names were mapped to Recon 2.2 [78,80]. StanDep was employed with the pre-processed expression data to identify core reactions active in the individual cells. To this end, enzyme expression was $\log_{10}$ transformed into a binary matrix with rows representing enzymes and columns as bins to identify minimum and maximum enzyme expression. A complete linkage metric with hierarchical clustering and Euclidean distance was used to cluster (number of clusters = 40) genes concerning their expression. Core reaction matrices were assembled, defined, and used as an input to fastcore [13] to reconstruct single-cell, context-specific metabolic models. The fastcore algorithm was employed to create cell-type-specific models based on the consistent Recon 2.2 model including the viral replication reaction and the list of core reactions from *StanDep* expanded by biomass objective function and VBOF. The reconstructed context-specific models for each cell are available from the BioModels database (see data availability).

For the analysis of metabolic pathway activity in the BALF2 data, reactions that have been found active in metabolic models of single cells were counted and summarized into 82 metabolic pathways based on the subsystem annotation of Recon 2.2. The small number of single-cell models with detected viral RNA were not considered to avoid confounding (87 of 148.420 cells). The resulting counts of active reactions per pathway were checked for too many single cells with zero counts, e.g., metabolic pathways were discarded if they showed zero counts in more than half of the single-cell models across all three patient groups (control, moderate and severe COVID). The remaining 57 metabolic pathways were statistically evaluated individually for their relation to patient groups while controlling for cell type ("Basal", "Ciliated," "Ciliated-dif", "FOXN4", "Ionocyte", "IRC", "outliers_epithelial", "Secretory", "Secretory-diff", "Squamous"). Active reaction counts were modeled as the dependent variable in negative binomial regressions (R-package MASS 7.3-57 function `glm.nb`[82]). Metabolic pathways with inflated zero counts were modeled with negative binomial regression with an additional zero-inflation model. The zero-inflation model took the same independent variables as the primary model, namely patient group and cell type (R-package pscl 1.5.5, function zeroinfl with dist="negbin"[83]). The logarithm to the base two was calculated for fold changes between the control group as baseline and any of the two COVID patient groups.

Prediction of viral replication capacity and antiviral targets

In order to predict viral replication capacity for a cell built from scRNA-Seq data, we used flux balance analysis [11] with the applied blood serum diet and maximized the flux through the VBOF. We performed single gene deletions to predict antiviral targets and assessed their effects on host biomass production and viral replication capacity. Gene knockouts, which were found to decrease viral replication capacity by at least 50% of the initial value while maintaining the host's biomass minimally at 80% of its initial value, were reported as tier-1 targets. Tier-2 targets reduced viral replication capacity by at least 50%, but decreased cellular biomass production by more than 20%. While the biomass reaction is typically used to predict maximal growth rates of cells, it consumes all the molecules whose production is continuously required to maintain cellular function and hence can be used as a proxy for metabolic requirements of normal cellular function. Examples of such cellular functions include, for instance, the production of amino acids for protein turnover, nucleotides for DNA repair, and energy equivalents for cellular function. For the identification of tier-1 and tier-2 targets, we considered only cells with a predicted viral replication rate above 0.01 mmol/gDW (unit of flux measurement in constraint-based models) and detected tier-1 targets. Moreover, we subsetted data to include only virally infected cells where possible (i.e. sufficient number of virally infected cells). Thus, for the cell culture data from SARS-CoV-2 infection (CALU3, scH1299) and the BALF1 data set, we only considered infected cells as indicated in the provided metadata. For the BALF2 data set, only few infected cells were detected. Since we observed priming of non-infected cells for viral replication upon viral infection of the host, we considered all SARS-CoV-2 permissive cell types of SARS-CoV-2 infected individuals for this dataset. For dengue and influenza A, we considered only cells with >0.1% of reads mapping to the respective viral genomes as indicated in the metadata provided along with the sequencing data.

For the comparison of known interaction partners of the viral proteome with tier-1 and tier-2 targets (Fig. 3), we subsetted tier-1 and tier-2 targets to those occurring in at least 5% of the cells for each data set for which tier-1 targets could be identified (high-confidence tier-1 and tier-2 targets, Supplementary Table S2). To identify broad-spectrum antiviral targets, we counted for each dataset and enzyme, how often it was listed as a tier-1 target. Additionally, we included information on known virus protein interactions [32–34]. For SARS-CoV-2, we used host proteins that had at least one reported interaction with a SARS-CoV-2 protein at a SAINTexpress Bayesian false-discovery rate (BFDR)<=0.05 [84] and an average spectral count >= 2. The list of considered interaction partners for each virus is provided in Supplementary Table S1. We derived a shortlist of candidate targets by subsetting the list to those enzymes listed as tier-1 targets at least once for each data set and reported as interaction partners of the proteome of at least two of the three viruses (39 candidates). The frequency at which each enzyme was listed as a tier-1 target is provided in Supplementary Table S5.

Further information from the literature, CRISPR-Cas studies [47,48,55] and the availability of suitable inhibitors were additionally used to identify candidate targets suitable for experimental testing. To identify the gene's relevance in other viral diseases, we searched the database of protein, genetic and chemical interactions (BioGRID)[35] and the molecular INTeraction database (MINT)[85]. To identify known drugs or inhibitors, we searched in the Drug Gene Interaction database (DGIdb) [86], the DrugBank database [87], and the GeneCards suite [88].

Statistical analysis

Statistical tests were performed with R version 4.1.3 if not indicated otherwise. The individual statistical tests are indicated for each case in which *p*-values are reported. In the case of multiple tests, false discovery rate control using the Benjamini and Hochberg procedure [89] implemented in the p.adjust function of R was used.

Experimental approaches

Cell culture

A549 cells (human alveolar basal epithelial adenocarcinoma) were maintained at 37°C with 5% CO_2 in RPMI 1640 Medium containing 10% (*v*/*v*) inactivated fetal calf serum (FCS) and 100 µg/mL penicillin-streptomycin.

Calu-3 cells (human lung adenocarcinoma) and HEp-2 cells (human epidermoid cancer cells) were maintained at 37°C with 5% CO_2 in Dulbecco's Modified Eagle Medium (DMEM) containing 10% FCS, GlutaMax, and 100 µg/mL penicillin-streptomycin.

CaCo-2 (human colorectal adenocarcinoma) and Huh7.5 cells (human hepatocellular carcinoma) were maintained at 37 °C with 5% CO_2 in DMEM containing 10% FCS, GlutaMax,
1% (*v*/*v*) nonessential amino acids and 100 µg/mL penicillin-streptomycin.

Viruses

Two different SARS-CoV-2 strains were used in this study. First is the recombinant SARS-CoV-2 clone expressing mNeonGreen icSARS-CoV-2 mNG [90]. It was obtained from the World Reference Center of Emerging Viruses and Arboviruses at the University of Texas Medical Branch (UTMB). For virus production, CaCo-2 cells were infected; 48 hours post-infection (hpi), the supernatant was collected, centrifuged, and stored at -80 °C. Second is a clinical SARS-CoV-2 isolate that belongs to the B.1.1.529 (omicron) BA.1 lineage. It was isolated from a PCR-positive patient by a throat swab at the Institute for Medical Virology and Epidemiology of Viral Diseases, University Hospital Tübingen (UKT). Briefly, 200 µL of patient material was used to inoculate CaCo-2 cells in a six-well plate (150,000/well). At 48 hpi, the supernatant was collected, centrifuged, and stored at -80 °C. After two consecutive passages, samples were prepared for NGS, and correct SARS-CoV-2 lineage was determined. The MOI was determined for both viruses by titration with serial dilutions. The number of infectious virus particles per mL was calculated as the (MOI × cell number)/(infection volume), where MOI = −ln(1 − infection rate). The recombinant Respiratory Syncytial Virus (RSV rA2-eGFP) was kindly provided by Konstantin Sparrer (Institute of Molecular Virology, University Hospital Ulm, Germany) and Michael N. Teng (University of South Florida Morsani College of Medicine, Tampa, Florida, USA) [91]. HEp-2 cells were infected, and the cells and the supernatant were harvested at 72 hpi, sonicated for 10 min at 35 °C, centrifuged, and stored at -80 °C to generate rA2-eGFP stocks. The recombinant influenza Virus A (IAV) expressing GFP (IAV-GFP SC35M) was kindly provided by Konstantin Sparrer (Institute of Molecular Virology, University Hospital Ulm, Germany) and Martin Schwemmle (Institute of Virology, University Hospital Freiburg, Germany)
[92].

doi:10.20944/preprints202210.0223.v1

For the dengue studies a recombinant dengue 2 strains 16681 (Genebank Accession NC_001474) containing a Renilla Luciferase Reporter was used [93]. The full-length dengue genome was transcribed as viral RNA and electroporated into Huh7.5 cells. 72 hours post electroporation the supernatant was collected, centrifuged and stored at -80 °C.

Compound information

Atpenin A5 (#sc-202475A) and Scyllo-Inositol (#sc-202808) were obtained from Santa Cruz Biotechnology (Dallas, Texas, USA) and dissolved in DMSO for atpenin A5 and in HPLC water for Scyllo-Inositol. Phenformin (#P7045-1G) and SR13800 (#5096630001) were purchased from Merck (Rahway, New Jersey, USA) and dissolved in HPLC water. Metformin (#AG-CR1-3689) was acquired from AdipoGen Life Sciences (San Diego, California, USA) and dissolved in HPLC water.

Initial screening of four drug candidates against SARS-CoV-2

CaCo-2 and Calu-3 cells were pre-treated with phenformin, SR13800, and scyllo-inositol in concentrations of 50 µM,

10 µM, and 2 µM, and atpenin A5 in concentrations of 10 µM, 2 µM, infection (MOI) = 0.2 for CaCo-2 cells and at a

MOI = 0.5 for Calu- --3-cells or mock-infected. After and 0.4 µM. After 24 hours, cells were infected with icSARS CoV

2 mNG [86] at a multiplicity of

48 hours post-infection (hpi), cells were fixed with 2% PFA and stained with Hoechst (1 µg / mL final concentration). Images of cell nuclei, mNeonGreen and bright field were taken with Cytation3 (Biotek, Winooski, VT, USA). Hoechst+ and mNeonGreen+ cells were counted by the Gen5 software (Biotek, Winooski, VT, USA), and infection rates were calculated using the ratio of mNeonGreen+/Hoechst+ cells.

IC_{50} calculation of phenformin, metformin, and atpenin A5

phenformin,$_{50}$ metformin, or atpenin A5. After 24 hours- cells were infected- with For IC calculations with the SARS-

CoV-2 strains, Calu 3 cells were pre treated with icSARS-CoV-2-mNG infected cells were fixed, stained, and measured

as described before.- - The icSARS CoV 2-mNG at a MOI = 0.5 or with SARS-CoV-2 Omicron at a MOI = 1.1. The

SARS-CoV-2 Omicron infected cells were fixed with 80% Acetone and stained by Immunofluorescence with rabbit

anti-SARS-CoV-2 nucleocapsid antibody and with goat AlexaFluor™ 594+ cells, and bright field were taken with the

Cytation3 (Biotek, Winooski, VT,anti rabbit AlexaFluor™ 594 antibody. Cell nuclei were stained with DAPI. Images

of cell nuclei,

USA), and DAPI+ and AlexaFluor™ 594+ cells were automatically counted by the Gen5 software (Biotek, Winooski, VT, USA).

For IC$_{50}$ calculations with dengue virus, phenformin or atpenin A5 were prediluted in Huh7.5 complete media and added to Huh7.5 cells one hour before adding the virus. At 24 hours post infection, lysis buffer was added to the cells, and the cell lysates were subjected to luciferase assay and measured with Cytation3 (Biotek, Winooski, VT, USA).
For IC$_{50}$ calculation with IAV or RSV, A549 cells were pre-treated with phenformin or atpenin A5. Cells were infected with IAV or RSV 24 hours post-treatment with a MOI of 0.6 (IAV), MOI of 1.4 (RSV), or mock-infected. After 24 hours (IAV) or 48 hours (RSV), cells were fixed with 2% PFA and stained with Hoechst. The plates were measured with Cytation3 (Biotek, Winooski, VT, USA), and Hoechst+ and GFP+ cells were counted by Gen5 software (Biotek, Winooski, VT, USA).
Prism 9 Software (GraphPad Software, Inc., San Diego, CA, USA, Version 9).$_{50}$ IC s of all viruses were calculated as the half maximal inhibitory dose using the GraphPad

CC$_{50}$ calculation of phenformin and atpenin A5

CC$_{50}$ calculations were performed using three methods to measure cell viability: the MTT assay, the CellTiter-Glo® assay (CTG), and monitoring cell viability via live cell imaging (IncuCyte®). For the MTT assay, Calu-3, Huh7.5 and A549 cells were treated with phenformin in concentrations of 6400 µM to 0.2 µM and atpenin A5 in concentrations of 640 µM to 0.15 µM in two-fold dilution. Atpenin A5 was dissolved in DMSO, therefore DMSO control with 1.3 % (≙ 640 µM Atpenin) was added to exclude false positive cell toxicity. The positive control is 50% DMSO to inhibit cell growth. Absorption levels at 570 nm and 650 nm wavelengths were measured, and values were normalized to non-treated cells. CC$_{50}$ was calculated as the half-maximal cytotoxic dose via GraphPad Prism 9 using four-parameter nonlinear regression. For CTG, Calu-3,
Huh7.5 and A549 cells were treated with the same concentrations as listed above and DMSO controls and positive control with 50% DMSO treated cells were added. Luminescent signals were measured by a Berthold TriStar2 S Multimode Reader. The data was then normalized to the non-treated control. CC$_{50}$ was calculated as the half-maximal cytotoxic dose via GraphPad Prism 9 using four-parameter nonlinear regression. For live cell imaging, Calu-3, Huh7.5 and A549 cells were treated with phenformin in concentrations of 12800 µM to 0.2 µM and atpenin A5 in concentrations of 640 µM to 0.15 µM in two-fold dilution. Plates were then stored in the IncuCyte® (Sartorius AG, Göttingen, Germany) at 37 °C with 5% CO$_2$. Cell confluence was measured every three to four hours via phase channel with 10x objective. For analysis, a basic analyzer of the IncuCyte® S3 Software (Sartorius AG, Göttingen, Germany) was used.

Acknowledgments

This work was supported by the BMBF-funded de.NBI Cloud within the German Network for Bioinformatics Infrastructure (de.NBI) (031A532B, 031A533A, 031A533B, 031A534A, 031A535A, 031A537A, 031A537B, 031A537C, 031A537D, 031A538A). CK acknowledges support by the Deutsche Forschungsgemeinschaft (DFG, German Research Foundation) within the cluster of excellence "Precision medicine in chronic inflammation" (DFG support code EXC2167), the collaborative research center "Metaorganisms" (DFG support code CRC1182), the research group miTarget (DFG support code FOR5042) and the German Ministry for Education and Research in the frame of iTREAT (BMBF support code 01ZX1902A). The DFG further supported this work under Germany's Excellence Strategy–EXC 2124–390838134 within the Cluster of Excellence CMFI (Controlling Microbes to Fight Infections). A.D. is funded by the Germany Center for Infection Research (DZIF) within the Deutsche Zentren der Gesundheitsforschung (BMBF-DZG, Germany Centers for Health Research of the Federal Ministry of Education and Research), grant no. 8020708703.

M.H. and M.B. were fellows of a MD stipend granted by the German Center for Infection Research (DZIF) under grant no. TI 07.003. The work is also funded by the BMBF and the Baden-Württemberg Ministry of Science as part of the Excellence Strategy of the German Federal and State Governments. We are grateful to Nantia Leonidou for helpful contributions. Some figures were created with BioRender.com.

Author contributions

A.R., A.D., and C.K, devised the computational component of the study. M.S. conceived and devised the experimental part of the study. A.R., M.H., J.J.S, A.D., M.S., and C.K. wrote the initial manuscript draft. A.R., J.J.S., L.B., C.K., G.M., and F.C. analyzed the computational data and contributed to the identification of antiviral compounds. M.H., M.B., J.D., R.J., and M.S., conducted all virus infection experiments as well as measurements of cellular metabolic activity and toxicity and analyzed the data. All authors contributed to manuscript editing and approved the final paper.

Competing interests

A.R., M.H., L.B., J.J.S., A.D., M.S., and C.K. have submitted a patent application for using phenformin and atpenin A5 as broad-spectrum antivirals.

Data availability

All data produced in the context of this work is available in the Supplementary Tables and Data. Scripts are available via GitHub in the repository https://github.com/draeger-lab/R-DRUGS. The human metabolic models with all constraints for the blood medium and the viral replication reactions for the individual viruses will become available in the form of COMBINE Archive files[94] (containing SBML[95,96] files Level 3 Version 1[97] with annotation[98] FBC extension version 2[99]) via BioModels Database[100].

Supplementary Information

Supplementary Figures

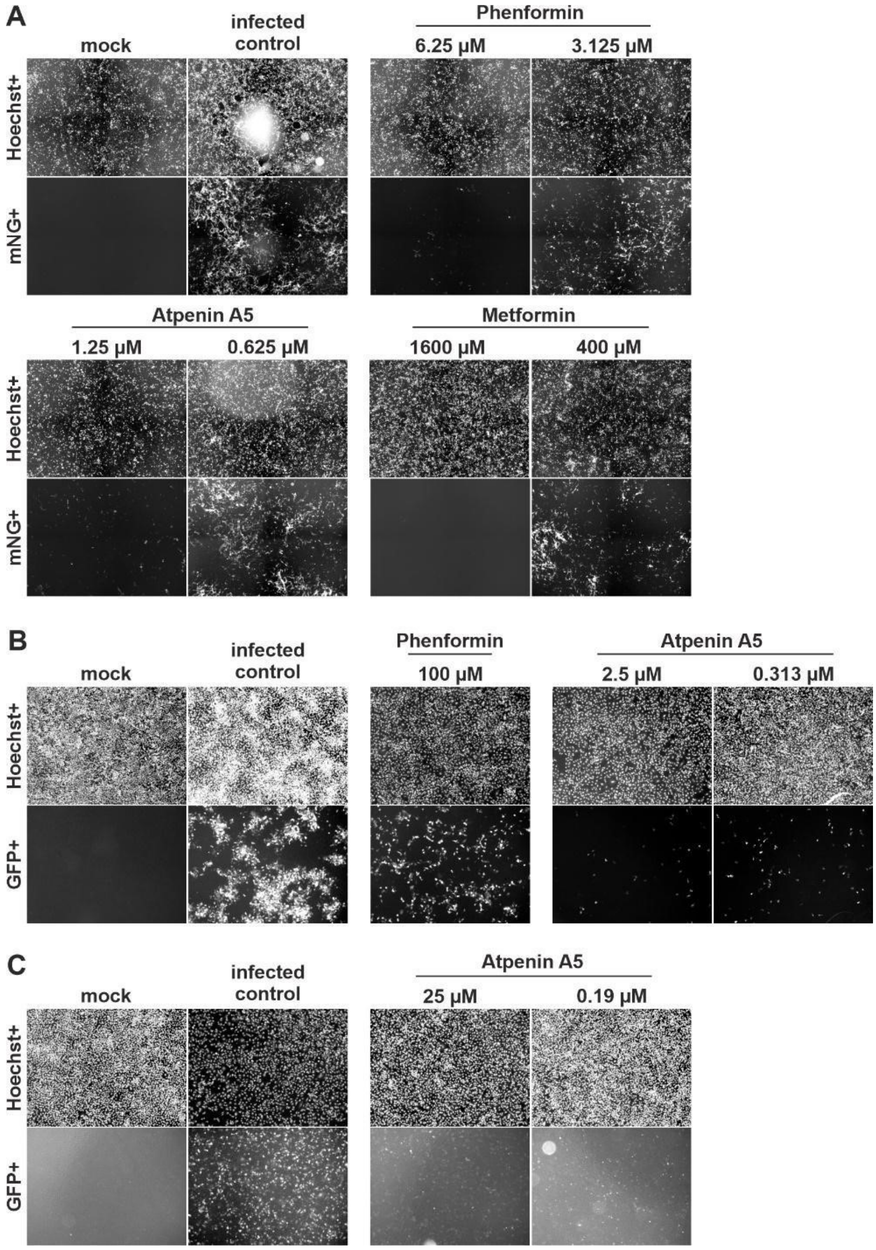

Supplementary Figure 1 | Primary data of infection experiments showing inhibition of SARS-CoV-2, RSV and IAV by atpenin A5, phenformin and metformin. Images show **A** Calu-3 cells infected with icSARS-CoV-2-mNG **B** A549 cells infected with respiratory syncytial virus and **C** A549 cells infected with influenza A virus treated with the indicated compounds and concentrations.

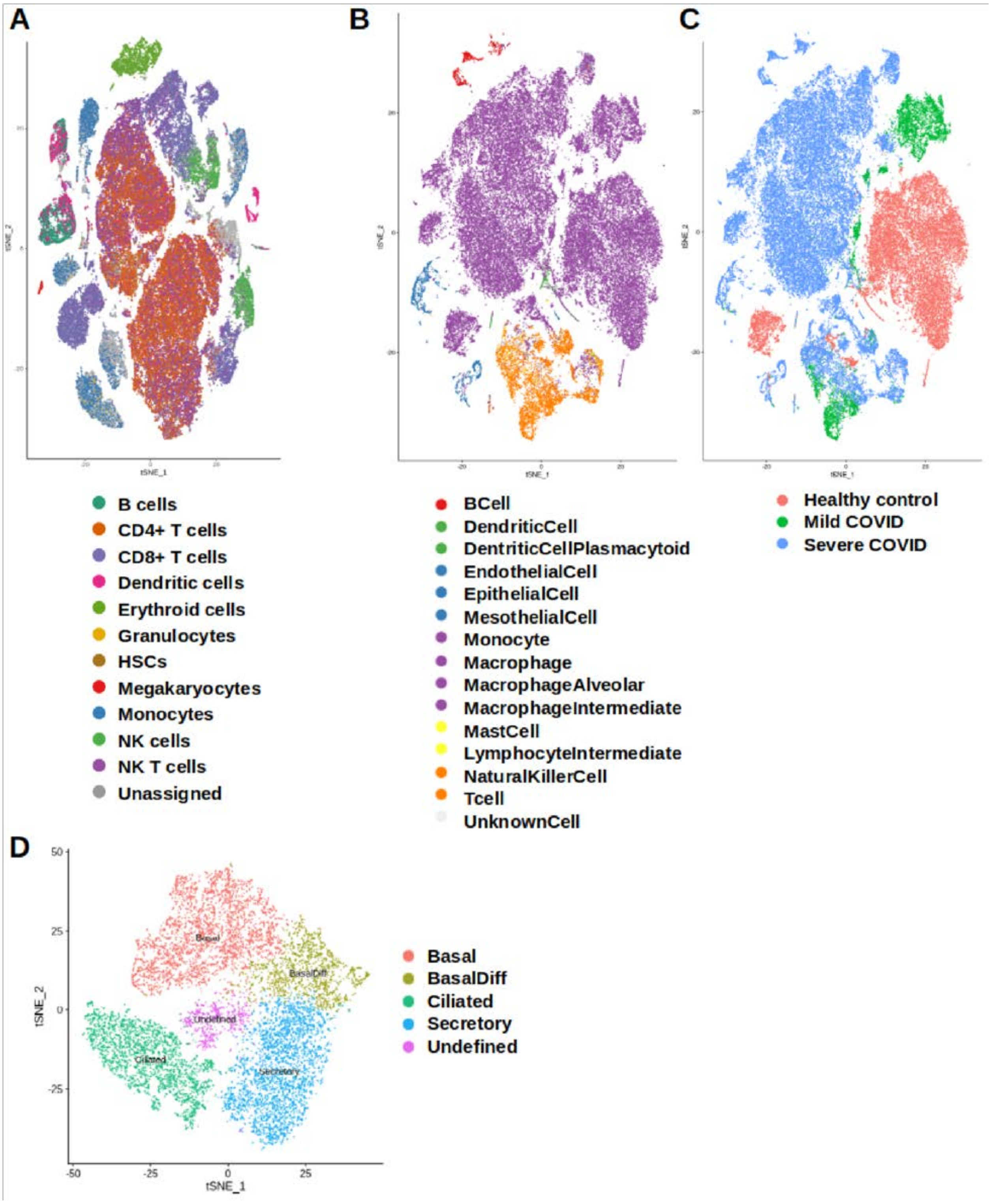

Supplementary Figure 2 | tSNE plots of cell types for the individual single-cell expression datasets of viral infection. Panels show (A) CHETAH-derived cell type annotation of the dengue dataset, based on a PBMC reference and (B) CHETAH-derived cell type annotation of the BALF1 dataset, based on a single cell lung atlas. Panel (C) shows the same tSNE-plot as (B) of the BALF1 dataset, but color coded for donors' health or COVID status. (D) Manual cell type annotation of the influenza H1N1 dataset.

doi:10.20944/preprints202210.0223.v1

Supplementary Tables

Supplementary Table S1 - Differentially active pathways in SARS-CoV-2 infected individuals
Supplementary Table S2 - Virus-host-interactions
Supplementary Table S3 - High-confidence tier-1 and tier-2 targets (Fig. 3)
Supplementary Table S4 - Frequency of tier-1 targets
Supplementary Table S5 - Broad-spectrum antiviral targets
Supplementary Table S6 - Viral protein copy numbers
Supplementary Table S7 - Viral replication reactions
Supplementary Table S8 - Blood Serum constraints
Supplementary Table S9 - Dengue dataset cell type annotation

Supplementary Data

Supplementary Data S1 - Viral replication rates, predicted tier-1/tier-2 targets and metadata for all reconstructed context-specific models.

References

1. Marty, A. M. & Jones, M. K. The novel Coronavirus (SARS-CoV-2) is a one health issue. *One Health* vol. 9 100123 Preprint at https://doi.org/10.1016/j.onehlt.2020.100123 (2020).
2. Azhar, E. I., Hui, D. S. C., Memish, Z. A., Drosten, C. & Zumla, A. The Middle East Respiratory Syndrome (MERS). *Infect. Dis. Clin. North Am.* **33**, 891–905 (2019).
3. Yang, W., Petkova, E. & Shaman, J. The 1918 influenza pandemic in New York City: age-specific timing, mortality, and transmission dynamics. *Influenza Other Respi. Viruses* **8**, 177–188 (2014).
4. Honigsbaum, M. Revisiting the 1957 and 1968 influenza pandemics. *Lancet* **395**, 1824–1826 (2020).
5. Arrizabalaga, J. The Black Death, 1346-1353: The Complete History (review). *Bulletin of the History of Medicine* vol. 80 161–163 Preprint at https://doi.org/10.1353/bhm.2006.0002 (2006).
6. Mora, C. *et al.* Over half of known human pathogenic diseases can be aggravated by climate change. *Nat. Clim. Chang.* 1–7 (2022).
7. Cutler, D. M. & Summers, L. H. The COVID-19 Pandemic and the $16 Trillion Virus. *JAMA* **324**, 1495–1496 (2020).
8. Shutters, S. T. Modelling long-term COVID-19 impacts on the U.S. workforce of 2029. *PLoS One* **16**, e0260797 (2021).
9. Geraghty, R. J., Aliota, M. T. & Bonnac, L. F. Broad-Spectrum Antiviral Strategies and Nucleoside Analogues. *Viruses* **13**, (2021).
10. Swainston, N. *et al.* Recon 2.2: from reconstruction to model of human metabolism. *Metabolomics* **12**, 109 (2016).
11. Renz, A., Widerspick, L. & Dräger, A. FBA reveals guanylate kinase as a potential target for antiviral therapies against SARS-CoV-2. *Bioinformatics* **36**, i813–i821 (2020).
12. Tabula Muris Consortium. A single-cell transcriptomic atlas characterizes ageing tissues in the mouse. *Nature* **583**, 590–595 (2020).

13. Vlassis, N., Pacheco, M. P. & Sauter, T. Fast reconstruction of compact context-specific metabolic network models. *PLoS Comput. Biol.* **10**, e1003424 (2014).
14. Zhu, Y., Wang, L., Yin, Y. & Yang, E. Systematic analysis of gene expression patterns associated with postmortem interval in human tissues. *Sci. Rep.* **7**, 5435 (2017).
15. Foulkes, A. S., Balasubramanian, R., Qian, J. & Reilly, M. P. Non-random sampling leads to biased estimates of transcriptome association. *Sci. Rep.* **10**, 6193 (2020).
16. Hu, F. *et al.* A compromised specific humoral immune response against the SARS-CoV-2 receptor-binding domain is related to viral persistence and periodic shedding in the gastrointestinal tract. *Cell. Mol. Immunol.* **17**, 1119–1125 (2020).
17. Rebendenne, A. *et al.* SARS-CoV-2 triggers an MDA-5-dependent interferon response which is unable to control replication in lung epithelial cells. *J. Virol.* (2021) doi:10.1128/JVI.02415-20.
18. Chen, L. *et al.* Detection of SARS-CoV-2 in saliva and characterization of oral symptoms in COVID-19 patients. *Cell Prolif.* **53**, e12923 (2020).
19. Zang, R. *et al.* TMPRSS2 and TMPRSS4 promote SARS-CoV-2 infection of human small intestinal enterocytes. *Sci Immunol* **5**, (2020).
20. Wang, Y. *et al.* Single-cell transcriptome analysis reveals differential nutrient absorption functions in human intestine. *J. Exp. Med.* **217**, (2020).
21. Ravindra, N. G. *et al.* Single-cell longitudinal analysis of SARS-CoV-2 infection in human airway epithelium identifies target cells, alterations in gene expression, and cell state changes. *PLoS Biol.* **19**, e3001143 (2021).
22. He, J. *et al.* Single-cell analysis reveals bronchoalveolar epithelial dysfunction in COVID-19 patients. *Protein & cell* vol. 11 680–687 (2020).
23. Perna, A. *et al.* Skin manifestations in COVID-19 patients, state of the art. A systematic review. *Int. J. Dermatol.* **60**, 547–553 (2021).
24. Wang, L. *et al.* A human three-dimensional neural-perivascular 'assembloid' promotes astrocytic development and enables modeling of SARS-CoV-2 neuropathology. *Nat. Med.* **27**, 1600–1606 (2021).
25. Ritchie, K. & Chan, D. The emergence of cognitive COVID. *World Psychiatry* **20**, 52–53 (2021).
26. Chua, R. L. *et al.* COVID-19 severity correlates with airway epithelium-immune cell interactions identified by single-cell analysis. *Nat. Biotechnol.* **38**, 970–979 (2020).
27. Liao, M. *et al.* Single-cell landscape of bronchoalveolar immune cells in patients with COVID-19. *Nat. Med.* **26**, 842–844 (2020).
28. Wyler, E. *et al.* Transcriptomic profiling of SARS-CoV-2 infected human cell lines identifies HSP90 as target for COVID-19 therapy. *iScience* **24**, 102151 (2021).
29. Medaglia, C. *et al.* A novel anti-influenza combined therapy assessed by single cell RNA-sequencing. Preprint at https://doi.org/10.1101/2021.07.27.453967.
30. Deprez, M. *et al.* A Single-Cell Atlas of the Human Healthy Airways. *Am. J. Respir. Crit. Care Med.* **202**, 1636–1645 (2020).
31. Zanini, F. *et al.* Virus-inclusive single-cell RNA sequencing reveals the molecular signature of progression to severe dengue. *Proc. Natl. Acad. Sci. U. S. A.* **115**, E12363–E12369 (2018).

32. Gordon, D. E. *et al.* A SARS-CoV-2 protein interaction map reveals targets for drug repurposing. *Nature* **583**, 459–468 (2020).

33. Shah, P. S. *et al.* Comparative Flavivirus-Host Protein Interaction Mapping Reveals Mechanisms of Dengue and Zika Virus Pathogenesis. *Cell* **175**, 1931–1945.e18 (2018).

34. Watanabe, T. *et al.* Influenza virus-host interactome screen as a platform for antiviral drug development. *Cell Host Microbe* **16**, 795–805 (2014).

35. Oughtred, R. *et al.* The BioGRID interaction database: 2019 update. *Nucleic Acids Res.* **47**, D529–D541 (2019).

36. Hu, M., Bogoyevitch, M. A. & Jans, D. A. Subversion of Host Cell Mitochondria by RSV to Favor Virus Production is Dependent on Inhibition of Mitochondrial Complex I and ROS Generation. *Cells* **8**, (2019).

37. Jäger, S. *et al.* Global landscape of HIV-human protein complexes. *Nature* **481**, 365–370 (2011).

38. Davis, Z. H. *et al.* Global mapping of herpesvirus-host protein complexes reveals a transcription strategy for late genes. *Mol. Cell* **57**, 349–360 (2015).

39. Rozenblatt-Rosen, O. *et al.* Interpreting cancer genomes using systematic host network perturbations by tumour virus proteins. *Nature* **487**, 491–495 (2012).

40. Tripathi, L. P. *et al.* Network based analysis of hepatitis C virus core and NS4B protein interactions. *Mol. Biosyst.* **6**, 2539–2553 (2010).

41. Martinez-Gil, L., Vera-Velasco, N. M. & Mingarro, I. Exploring the Human-Nipah Virus Protein-Protein Interactome. *J. Virol.* **91**, (2017).

42. Kelly, B., Tannahill, G. M., Murphy, M. P. & O'Neill, L. A. J. Metformin Inhibits the Production of Reactive Oxygen Species from NADH:Ubiquinone Oxidoreductase to Limit Induction of Interleukin-1β (IL-1β) and Boosts Interleukin-10 (IL-10) in Lipopolysaccharide (LPS)-activated Macrophages. *J. Biol. Chem.* **290**, 20348–20359 (2015).

43. Crouse, A. B. *et al.* Metformin Use Is Associated With Reduced Mortality in a Diverse Population With COVID-19 and Diabetes. *Front. Endocrinol.* **11**, 600439 (2020).

44. Sterne, J. [Report on 5-years' experience with dimethylbiguanide (metformin, glucophage) in diabetic therapy]. *Wien. Med. Wochenschr.* **113**, 599–602 (1963).

45. Sogame, Y., Kitamura, A., Yabuki, M. & Komuro, S. A comparison of uptake of metformin and phenformin mediated by hOCT1 in human hepatocytes. *Biopharm. Drug Dispos.* **30**, 476–484 (2009).

46. Germain, M.-A. *et al.* Elucidating novel hepatitis C virus-host interactions using combined mass spectrometry and functional genomics approaches. *Mol. Cell. Proteomics* **13**, 184–203 (2014).

47. Daniloski, Z. *et al.* Identification of Required Host Factors for SARS-CoV-2 Infection in Human Cells. *Cell* **184**, 92–105.e16 (2021).

48. Wang, R. *et al.* Genetic Screens Identify Host Factors for SARS-CoV-2 and Common Cold Coronaviruses. *Cell* **184**, 106–119.e14 (2021).

49. Morris, M. E. & Felmlee, M. A. Overview of the proton-coupled MCT (SLC16A) family of transporters: characterization, function and role in the transport of the drug of abuse gamma-hydroxybutyric acid. *AAPS J.* **10**, 311–321 (2008).

50. Doherty, J. R. *et al.* Blocking lactate export by inhibiting the Myc target MCT1 Disables glycolysis and glutathione synthesis. *Cancer Res.* **74**, 908–920 (2014).
51. de Chassey, B. *et al.* The interactomes of influenza virus NS1 and NS2 proteins identify new host factors and provide insights for ADAR1 playing a supportive role in virus replication. *PLoS Pathog.* **9**, e1003440 (2013).
52. Zhu, S.-L. *et al.* Inducible CYP4F12 enhances Hepatitis C virus infection via association with viral nonstructural protein 5B. *Biochem. Biophys. Res. Commun.* **471**, 95–102 (2016).
53. Horsefield, R. *et al.* Structural and computational analysis of the quinone-binding site of complex II (succinate-ubiquinone oxidoreductase): a mechanism of electron transfer and proton conduction during ubiquinone reduction. *J. Biol. Chem.* **281**, 7309–7316 (2006).
54. Wojtovich, A. P. & Brookes, P. S. The complex II inhibitor atpenin A5 protects against cardiac ischemia-reperfusion injury via activation of mitochondrial KATP channels. *Basic Res. Cardiol.* **104**, 121–129 (2009).
55. Wei, J. *et al.* Genome-wide CRISPR Screens Reveal Host Factors Critical for SARS-CoV-2 Infection. *Cell* **184**, 76–91.e13 (2021).
56. Muller, M. *et al.* Large scale genotype comparison of human papillomavirus E2-host interaction networks provides new insights for e2 molecular functions. *PLoS Pathog.* **8**, e1002761 (2012).
57. Barbosa, J. A. F., Sparapani, S., Boulais, J., Lodge, R. & Cohen, É. A. Human Immunodeficiency Virus Type 1 Vpr Mediates Degradation of APC1, a Scaffolding Component of the Anaphase-Promoting Complex/Cyclosome. *J. Virol.* **95**, e0097120 (2021).
58. Chen, X., Ji, Z. L. & Chen, Y. Z. TTD: Therapeutic Target Database. *Nucleic Acids Res.* **30**, 412–415 (2002).
59. Michon, C. *et al.* A bacterial cell factory converting glucose into scyllo-inositol, a therapeutic agent for Alzheimer's disease. *Commun Biol* **3**, 93 (2020).
60. Wang, X. *et al.* Fecal viral shedding in COVID-19 patients: Clinical significance, viral load dynamics and survival analysis. *Virus Res.* **289**, 198147 (2020).
61. Al Nemer, A. Histopathologic and Autopsy Findings in Patients Diagnosed With Coronavirus Disease 2019 (COVID-19): What We Know So Far Based on Correlation With Clinical, Morphologic and Pathobiological Aspects. *Adv. Anat. Pathol.* **27**, 363–370 (2020).
62. Bernardes, J. P. *et al.* Longitudinal Multi-omics Analyses Identify Responses of Megakaryocytes, Erythroid Cells, and Plasmablasts as Hallmarks of Severe COVID-19. *Immunity* **53**, 1296–1314.e9 (2020).
63. Lee, S. *et al.* Virus-induced senescence is a driver and therapeutic target in COVID-19. *Nature* **599**, 283–289 (2021).
64. Elesela, S. & Lukacs, N. W. Role of Mitochondria in Viral Infections. *Life* **11**, (2021).
65. Stang, M., Wysowski, D. K. & Butler-Jones, D. Incidence of lactic acidosis in metformin users. *Diabetes Care* **22**, 925–927 (1999).
66. Nattrass, M., Sizer, K. & Alberti, K. G. Correlation of plasma phenformin concentration with metabolic effects in normal subjects. *Clin. Sci.* **58**, 153–155 (1980).
67. LaMoia, T. E. *et al.* Metformin, phenformin, and galegine inhibit complex IV activity and reduce glycerol-derived gluconeogenesis. *Proc. Natl. Acad. Sci. U. S. A.* **119**, e2122287119 (2022).

68. Miyadera, H. *et al.* Atpenins, potent and specific inhibitors of mitochondrial complex II (succinate-ubiquinone oxidoreductase). *Proc. Natl. Acad. Sci. U. S. A.* **100**, 473–477 (2003).
69. Zhao, T., Mu, X. & You, Q. Succinate: An initiator in tumorigenesis and progression. *Oncotarget* **8**, 53819–53828 (2017).
70. Wang, H. *et al.* Synthesis and Antineoplastic Evaluation of Mitochondrial Complex II (Succinate Dehydrogenase) Inhibitors Derived from Atpenin A5. *ChemMedChem* **12**, 1033–1044 (2017).
71. Mayer, K. A., Stöckl, J., Zlabinger, G. J. & Gualdoni, G. A. Hijacking the Supplies: Metabolism as a Novel Facet of Virus-Host Interaction. *Front. Immunol.* **10**, 1533 (2019).
72. Adams, T. S. *et al.* Single-cell RNA-seq reveals ectopic and aberrant lung-resident cell populations in idiopathic pulmonary fibrosis. *Sci Adv* **6**, eaba1983 (2020).
73. Aller, S., Scott, A., Sarkar-Tyson, M. & Soyer, O. S. Integrated human-virus metabolic stoichiometric modelling predicts host-based antiviral targets against Chikungunya, Dengue and Zika viruses. *J. R. Soc. Interface* **15**, (2018).
74. Li, W. *et al.* RefSeq: expanding the Prokaryotic Genome Annotation Pipeline reach with protein family model curation. *Nucleic Acids Res.* **49**, D1020–D1028 (2021).
75. de Kanter, J. K., Lijnzaad, P., Candelli, T., Margaritis, T. & Holstege, F. C. P. CHETAH: a selective, hierarchical cell type identification method for single-cell RNA sequencing. *Nucleic Acids Res.* **47**, e95 (2019).
76. Clough, E. & Barrett, T. The Gene Expression Omnibus Database. *Methods in Molecular Biology* 93–110 Preprint at https://doi.org/10.1007/978-1-4939-3578-9_5 (2016).
77. Butler, A., Hoffman, P., Smibert, P., Papalexi, E. & Satija, R. Integrating single-cell transcriptomic data across different conditions, technologies, and species. *Nat. Biotechnol.* **36**, 411–420 (2018).
78. Joshi, C. J. *et al.* StanDep: Capturing transcriptomic variability improves context-specific metabolic models. *PLoS Comput. Biol.* **16**, e1007764 (2020).
79. Howe, K. L. *et al.* Ensembl 2021. *Nucleic Acids Res.* **49**, D884–D891 (2021).
80. Cunningham, F. *et al.* Ensembl 2019. *Nucleic Acids Res.* **47**, D745–D751 (2019).
81. Zaffagni, M. *et al.* SARS-CoV-2 Nsp14 mediates the effects of viral infection on the host cell transcriptome. *Elife* **11**, (2022).
82. Venables, W. N. & Ripley, B. D. *Modern AppliedStatistics with S*. (Springer, 2012).
83. Zeileis, A., Kleiber, C. & Jackman, S. Regression Models for Count Data in *R*. *Journal of Statistical Software* vol. 27 Preprint at https://doi.org/10.18637/jss.v027.i08 (2008).
84. Teo, G. *et al.* SAINTexpress: improvements and additional features in Significance Analysis of INTeractome software. *J. Proteomics* **100**, 37–43 (2014).
85. Licata, L. *et al.* MINT, the molecular interaction database: 2012 update. *Nucleic Acids Res.* **40**, D857–61 (2012).
86. Cotto, K. C. *et al.* DGIdb 3.0: a redesign and expansion of the drug-gene interaction database. *Nucleic Acids Res.* **46**, D1068–D1073 (2018).
87. Wishart, D. S. *et al.* DrugBank 5.0: a major update to the DrugBank database for 2018. *Nucleic Acids Res.* **4 6**, D1074–D1082 (2018).

88. Stelzer, G. *et al.* The GeneCards Suite: From Gene Data Mining to Disease Genome Sequence Analyses. *Curr. Protoc. Bioinformatics* **54**, 1.30.1–1.30.33 (2016).
89. Benjamini, Y. & Hochberg, Y. Controlling the False Discovery Rate: A Practical and Powerful Approach to Multiple Testing. *Journal ofthe Royal Statistical Society: Series B (Methodological)* vol. 57 289–300 Preprint at https://doi.org/10.1111/j.2517-6161.1995.tb02031.x (1995).
90. Xie, X. *et al.* An Infectious cDNA Clone of SARS-CoV-2. *Cell Host Microbe* **27**, 841–848.e3 (2020).
91. Villenave, R. *et al.* Induction and Antagonism of Antiviral Responses in Respiratory Syncytial Virus-Infected Pediatric Airway Epithelium. *J. Virol.* **89**, 12309–12318 (2015).
92. Reuther, P. *et al.* Generation of a variety of stable Influenza A reporter viruses by genetic engineering of the NS gene segment. *Sci. Rep.* **5**, 11346 (2015).
93. Fischl, W. & Bartenschlager, R. High-throughput screening using dengue virus reporter genomes. *Methods Mol. Biol.* **1030**, 205–219 (2013).
94. Bergmann, F.T. *et al*. COMBINE archive and OMEX format: one file to share all information to reproduce a modeling project. *BMC Bioinformatics* 15:369. https://doi.org/10.1186/ s12859-014-0369-z (2014).
95. Keating, S. M. *et al*. SBML Level 3: an extensible format for the exchange and reuse of biological models. *Mol. Syst. Biol.* 16, e9110. https://doi.org/10.15252/msb.20199110 (2020).
96. Renz, A. *et al*. Clinical applications of metabolic models in SBML format. In: *Systems Medicine*, Vol. 3, ed O. Wolkenhauer, 362-371. https://doi.org/10.1016/ B978-0-12-801238-3.11524-7 (2020).
97. Hucka, M. *et al.* The Systems Biology Markup Language (SBML): Language Specification for Level 3 Version 2 Core Release 2. *J. Integr. Bioinform*. 15, 1. https://doi.org/10.1515/ jib-2019-0021 (2019).
98. Neal, M. L. *et al.* Harmonizing semantic annotations for computational models in biology. *Brief. Bioinform.* 20, 540-550. https://doi.org/10.1093/bib/bby087 (2018).
99. Olivier, B. G. & Bergmann, F. T. SBML Level 3 package: Flux Balance Constraints version 2. *J. Integr. Bioinform.* 15:20170082. https://doi.org/10.1515/jib-2017-0082 (2018).
100. Malik-Sheriff, R. S. *et al.* BioModels—15 years of sharing computational models in life science. *Nucleic Acids Res.* 48, D407-D415. https://doi.org/10.1093/nar/gkz1055 (2020).